Observed Characteristics of the MJO Relative to Maximum Rainfall

JAMES J. BENEDICT AND DAVID A. RANDALL

Department of Atmospheric Science, Colorado State University, Fort Collins, Colorado

(Manuscript received 14 November 2005, in final form 13 October 2006)

ABSTRACT

This study examines various dynamical and thermodynamical processes that characterize the Madden–Julian oscillation (MJO). Episodes of deep convection related to the MJO based on rainfall data from the Tropical Rainfall Measuring Mission (TRMM) satellite and the Global Precipitation Climatology Project (GPCP) are identified. Although broad convective envelopes are located utilizing spectrally filtered precipitation, analyses of the features within the envelopes are carried out using unfiltered rainfall and 40-yr ECMWF Re-Analysis (ERA-40) fields. The events are composited and categorized based on geographic location and relative intensity.

The composited fields illustrate that, prior to the onset of deep convection, shallow cumulus and cumulus congestus clouds are actively involved in vertical convective transport of heat and moisture. Drying, first accomplished immediately following deep convection in the lower troposphere, is associated with an enhanced horizontal (westerly) advective component and may be related to mesoscale processes. Drying related to deep-layer subsidence is delayed until one to two weeks following intense rainfall. The importance of gradual lower-tropospheric heating and moistening and the vertical transport of energy and moisture are shown in a comparison of vigorous and weak MJO events. Additionally, a comparison of the composite fields to proposed wave instability theories suggests that certain theories are effective in explaining specific phases of the disturbance, but no single theory can yet explain all aspects of the MJO. The discharge–recharge and frictional moisture convergence mechanisms are most relevant for explaining many of the observed features of MJO evolution.

1. Introduction

The Madden–Julian oscillation (MJO), an equatorial disturbance first noted in the early 1970s (Madden and Julian 1971, 1994), involves multiscale cloud and precipitation processes and is manifested in numerous atmospheric variables. Despite decades of research, the combination of a poor representation of this tropical feature in most current general circulation models (GCMs) and a lack of comprehensive understanding of several of its mechanisms highlights the need for continued exploration of the MJO. This report utilizes a host of observational and reanalysis datasets to focus on the precipitation, convective, and advective processes both before and after MJO-related deep convection.

A number of studies have provided valuable insights into the structure and associated physical mechanisms of the MJO [see reviews in Lau and Waliser (2005) and Zhang (2005)]. In particular, the general characteristics and life cycle of the MJO as seen in a number of atmospheric variables have been researched (Hendon and Salby 1994; DeMott and Rutledge 1998; Maloney and Hartmann 1998; Myers and Waliser 2003; Kiladis et al. 2005, hereafter KSH05). The convective and stratiform cloud and precipitation processes during the MJO's wet phase have also been investigated (Lin and Johnson 1996a,b; Houze et al. 2000; Kikuchi and Takayabu 2004). Several other studies have focused on convective time scales, the regional environment within which wave initiation occurs in the Indian Ocean, and what related mechanisms might be important (Bladé and Hartmann 1993; Hu and Randall 1994; Kemball-Cook and Weare 2001). Lagged-regression and correlation studies utilizing OLR-based indices and additional datasets have advanced our knowledge of the vertical and temporal structure of the MJO (Woolnough et al. 2000; Sperber 2003). Straub and Kiladis (2003) examined the observed structure of convectively coupled

Corresponding author address: James J. Benedict, Department of Atmospheric Science, Colorado State University, Fort Collins, CO 80523.
E-mail: jim@atmos.colostate.edu

DOI: 10.1175/JAS3968.1

Kelvin waves, a type of wave that shares features with the MJO. Recently, the study of Bony and Emanuel (2005), which employed a simplified atmospheric model to examine the relationships between moisture, radiation, and convection, highlighted the importance of moist processes involved in obtaining realistic wave growth and propagation speeds of intraseasonal tropical disturbances.

The purpose of this study is to explore certain features of the MJO—particularly the influence of shallow cumuli and cumulus congestus prior to intense convection as well as lower-tropospheric drying following the heavy rainfall—using analyses of composites based on hydrological data from the Tropical Rainfall Measuring Mission (TRMM) and the Global Precipitation Climatology Project (GPCP). What role do these cloud types play as the MJO wet phase propagates eastward, and what is the time scale on which MJO-related shallow cumulus processes act? Are there differences in the nature of tropospheric heating and moistening based on the geographic location or relative intensity of the disturbance? Which mechanisms are important during the onset of low-level drying following deep convection? To answer these questions, we conduct an examination of cloud and advective processes, as gathered from reanalysis datasets, which are associated with the time-evolving MJO event at fixed geographic locations. Composite results presented here are also compared with proposed wave instability theories including conditional instability of the second kind associated with large-scale tropical waves (wave-CISK; Hayashi 1970; Lindzen 1974), wind-evaporation feedback (e.g., Emanuel 1987; Wang 1988; Jones and Weare 1996), stratiform instability (Mapes 2000), the frictional–convergence feedback (Wang 1988; Maloney and Hartmann 1998), and the discharge–recharge mechanism (Bladé and Hartmann 1993; Hu and Randall 1994; Kemball-Cook and Weare 2001).

This analysis involves a new approach to identify MJO events. Several previous studies (Hendon and Salby 1994; Maloney and Hartmann 1998; Sperber 2003; Lin et al. 2005; KSH05) have primarily utilized linear regression or EOF techniques. In the current study, spectrally filtered rainfall data are implemented solely to locate MJO-related convective envelopes, while unfiltered rainfall and 40-yr European Centre for Medium-Range Weather Forecasts (ECMWF) Re-Analysis (ERA-40) data fields are used to examine salient features within these envelopes. We adopt this approach in order to balance resolution with statistical clarity concerning the observed physical features, namely suppressed-phase shallow cumulus growth and lower-tropospheric drying following the heaviest rainfall.

This study is one of the first to examine MJO composite events based on TRMM rainfall using a wide range of dynamic and thermodynamic reanalysis variables. We selected rainfall as the variable on which events are based because of its strong ties to the MJO deep convection. Cho et al. (2004) used TRMM data to explore the spectral characteristics of tropical disturbances, including the MJO. Morita et al. (2006) implemented TRMM data to examine convective and stratiform rainfall and latent heating structures of the MJO. Additionally, the TRMM-based study by Masunaga et al. (2006) underscores the structural complexity and importance of wave interactions within the MJO convective envelope, illustrating the usefulness of combining unfiltered data fields with guidance based on filtered signals.

The various data sources utilized in this study are discussed in section 2. Section 3 outlines statistical methods that are applied to the data. We display time–height composites of several fundamental variables in section 4, and convective and advective processes related to the MJO are examined in section 5. Section 6 contains results from an analysis of the MJO using an extended data record and discusses the relevance of our findings to proposed wave instability theories of the MJO. Concluding remarks are given in section 7.

2. Data sources

The present study is based primarily on four data sources: TRMM, GPCP, ERA-40, and the Moderate Resolution Imaging Spectroradiometer–*Terra* satellite (MODIS–*Terra*). Table 1 outlines the specifications of these main datasets.

The primary source for precipitation data is the TRMM satellite. The TRMM combined $1° \times 1°$ rainfall product 3B42 is derived from a number of spaceborne instruments (see Kummerow et al. 2000). TRMM's precipitation radar provides a high degree of rainfall resolution and accuracy. This, combined with improved passive microwave and visible/infrared instrumentation as well as a sufficiently long data record (8+ yr), offers the opportunity to study composited MJO events using direct precipitation measurements. Unless otherwise noted, the results shown in this study use 5-day (pentad) averages of all datasets. We found the pentad-averaged datasets provide results that are more easily interpreted and statistically robust (owing to the small sample size of the TRMM data), despite some loss of temporal resolution.

Pentad GPCP total precipitation (Huffman et al.

TABLE 1. Primary data sources used in this study.

	TRMM (3B42)	GPCP	ERA-40	MODIS
Origin/platform	Satellite (TRMM)	Rain gauge and satellite data	Observations and model forecasts	Satellite (*Terra*)
Horizontal resolution	1° × 1°	2.5° × 2.5°	2.5° × 2.5°	1° × 1°
Chosen temporal domain	1 Jan 1998–28 Feb 2004	1 Jan 1984–31 May 2002	1 Jan 1984–31 May 2002	1 Jan 1998–28 Feb 2004
Vertical levels	Surface	Surface	1000, 925, 850, 775, 700, 600, 500, 400, 300, 250, 200 hPa	Single level
Variables	Total precipitation	Total precipitation	Dynamic, thermodynamic, and radiative variables	Cloud-top temperature and pressure

2001) extending from 1984–2001 is used as a second rainfall data source. These data compare favorably with TRMM, displaying a temporal correlation of 0.9 for most warm-ocean equatorial areas. The GPCP rainfall is used in combination with ERA-40 data records of similar time span to examine MJO events prior to the beginning of the TRMM record. More events are observed in the longer GPCP record, allowing subdivisions based on geographic location and relative event strength as will be discussed in section 6a.

Pentad 2.5° × 2.5° ERA-40 data are used to describe dynamic, thermodynamic, and radiative atmospheric states during the selected period of analysis. The ECMWF reanalysis dataset provides complete data coverage over an area where direct observations are sparse, namely the Indian and West Pacific Oceans. This advantage is counteracted by the sensitivity of the reanalyses to parameterizations, notably in data-sparse areas. Several issues related to sensitivities of observations, data assimilation, and/or model parameterizations are listed in Table 2, along with some examples of alternative datasets that might satisfy the requirements of the current study in terms of the spatial and temporal domain. Correlations of MJO composite time series for near-surface Quick Scatterometer (QuikSCAT) and ERA-40 zonal winds are statistically significant above

TABLE 2. A list of some ERA-40 variables and their associated issues in relation to the current study. Examples of alternative datasets appear in the third column. The proposed alternative datasets are, whenever possible, independent of the ERA-40 dataset (e.g., not assimilated). These alternative datasets must also be applicable to the current study in terms of spatial and temporal domains.

ERA-40 variable	ERA-40 issue	Example(s) of alternative data sources	Comments
u, v	Slightly overestimated over open tropical oceans and underestimated over isolated island locations[a]	QuikSCAT (surface winds), radiosonde datasets[c] [Integrated Global Radiosonde Archive (IGRA)]	Composite ERA-40 and QuikSCAT surface winds compare favorably; low observation density over Indian Ocean for IGRA
ω	Constrained to model parameterizations, especially in regions of convection[b]	None applicable to current study	
T	Slight climatological warm (cool) bias in lower (upper) tropical troposphere[a]	Radiosonde datasets[c] (IGRA)	Few observations over Indian Ocean for IGRA
Moisture (q, PW)	Slight overestimation of boundary layer q due to overestimated SLHF and turbulent vertical moisture transport[a]	MODIS, radiosonde datasets[c] (IGRA)	Few observations over Indian Ocean for IGRA
OLR	Constrained to data assimilation scheme and radiative transfer model[b]	CERES or ERBE radiances	Composite ERA-40 and CERES OLR compare reasonably well
SLHF	Constrained to bulk aerodynamic parameterizations, overestimated over tropical oceans due to biases in ship observations of near-surface winds[a,b]	None applicable to current study	

[a] The review in Källberg (1998) addresses deficiencies in the 15-yr ECMWF Re-Analysis.
[b] ERA-40 model documentation (ECMWF 2003a,b).
[c] Select radiosonde data are assimilated into ERA-40.

the 95% level; the same is true for a comparison of composite OLR from ERA-40 and the Clouds and Earth's Radiant Energy (CERES) project. Although our nonprecipitation results are based on ERA-40 (which does not assimilate TRMM data), we are comforted by how well the composited ERA-40 dynamical and thermodynamical fields match up with the composited TRMM precipitation profile. For example, maxima in ERA-40-derived deep convective heating and vertical motion occur simultaneously with the peak in composited TRMM rainfall for MJO disturbances.

We also utilize cloud-top pressure (CTP) and temperature (CTT) from the MODIS–*Terra* MOD08-D3 $1° \times 1°$ dataset. Although the accuracy of CTP for multiple cloud layers is uncertain, CTP values for nonoverlapping clouds above 700 hPa are accurate to within 50 hPa [see Platnick et al. (2003) and King et al. (2003) for reviews].

3. Methodology

A number of statistical tools, outlined in Fig. 1, are applied to the data. To isolate features that are related to the MJO, we spectrally analyze and filter total precipitation in zonal wavenumber and frequency space. Distinct intraseasonal convective events associated with the MJO are composited based on maximum rainfall. From these composites, we derive additional statistical parameters.

Our spectral analysis of total precipitation follows the procedure of Wheeler and Kiladis (1999). Although they spectrally analyze OLR in the wavenumber-frequency domain (their Fig. 3), our results based on precipitation are very similar (not shown). In addition to spectral analysis, we also implement filtering methods to extract particular wave features from the data. Despite the high degree of spatial and temporal variability of equatorial rainfall, we find that the larger-scale rain structures, especially when averaged meridionally, are captured reasonably well by spectral filtering over the periods and wavenumbers of interest.

To obtain the MJO-filtered data, we isolate signals characterized by eastward-propagating disturbances of zonal wavenumber 1–5 and period 20–100 days. For comparison, Wheeler and Kiladis (1999) use wavenumbers 1–5 and periods 30–96 days, and Kemball-Cook and Weare (2001) effectively retain wavenumbers 1–6 and periods 10–100 days as spectral bounds appropriate for MJO filtering. Versions of the MJO-filtered dataset are used to (i) distinguish individual convective events associated with the MJO and (ii) construct a composite MJO event. We analyze the convective events using

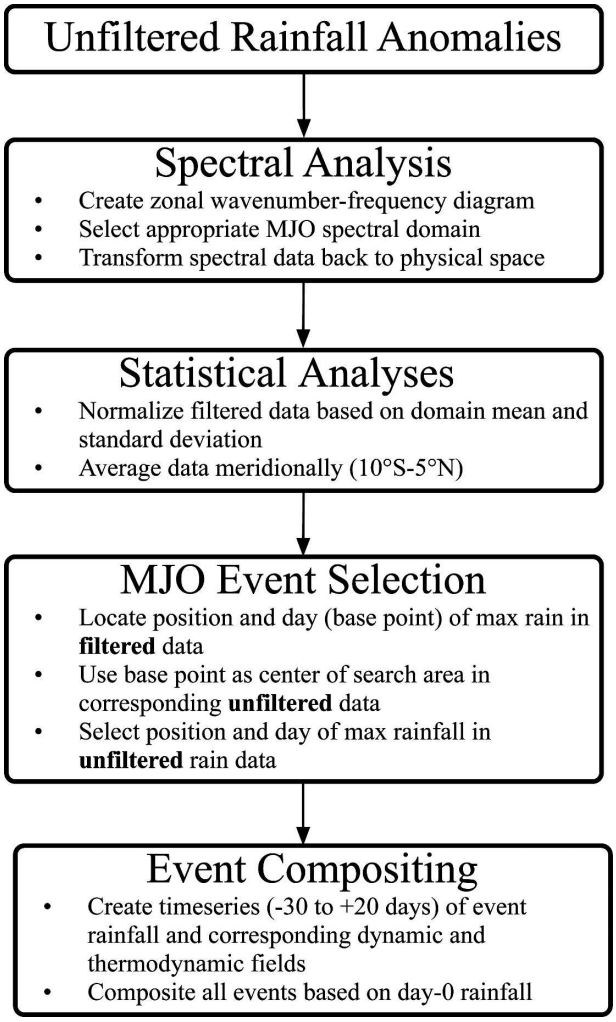

FIG. 1. Flow diagram of the MJO event selection and compositing process.

time series of meridionally averaged (10°S–5°N) rainfall anomalies at a particular longitude.

The MJO-filtered data are standardized based on an area-averaged mean and standard deviation (10°S–5°N, 0°–360°). This procedure brings into focus rainfall events in the highly variable tropical Indian and west Pacific Oceans, while deemphasizing signals not associated with the MJO outside this region. We then construct Hovmöller diagrams (10°S–5°N) of the standardized data. Individual convective events are defined according to a stringent set of criteria, similar to the constraints imposed by Rui and Wang (1990). To qualify as an MJO convective episode, the standardized, MJO-filtered rainfall anomaly (R) in the Hovmöller diagram must exceed 1σ in magnitude across a 20° longitudinal extent throughout its lifetime, which must be a minimum of 15 days. During its lifetime,

R must also exceed 1.5σ at any point. The event must occur in the Indian or west Pacific Ocean region (50°E–170°W) during the boreal nonsummer months (15 September–31 May). The 16 MJO convective events (from TRMM data) that satisfy these constraints are visually checked by comparison with Hovmöller diagrams of unfiltered TRMM rainfall.

A goal of this paper is the exploration of the atmospheric dynamics and cloud characteristics during the developmental and decaying stages of the MJO. The processes of interest occur on spatial and temporal scales that might be eliminated by excessive spectral filtering or regression techniques. In an attempt to include these convective processes under the umbrella of the larger-scale MJO, we use the identified events based on R simply as a guide. For each event, the longitude and time of maximum R are recorded. This longitude and time become the center point of a search area using an identical Hovmöller diagram (10°S–5°N) of unfiltered rainfall. We devise this search area, which scans ±15° longitude and ±5 days for the maximum meridionally averaged rainfall value, based on the idea that the date and location of the filtered precipitation maximum often are not exactly collocated with their unfiltered counterparts. The composite results are not strongly sensitive to adjustments in the search area. Following the search procedure, the resulting longitude and time of the unfiltered rainfall maximum define the base point (lag day 0) of the event, upon which all other variables are centered. The base point time series, which represent the evolution of some meridionally averaged variable at fixed longitude, are analyzed from 30 days prior to rain maximum (lag −30) to 20 days after rain maximum (lag +20). We then construct time–height cross sections of all variables for all MJO events identified, and these events are composited. The final composites are converted into anomaly forms, defined as departures from the mean atmospheric state during an MJO convective event (see appendix). Briefly, the mean atmospheric state characterizes the expected background environment in which MJO convective events take place. This state is calculated by averaging a variable at fixed pressure over all appropriate lag days (−30 to +20) or pentads (−6 to +4) for all events, resulting in a single background value for each pressure level. For each lag time and pressure level, anomalies are defined as departures from this background value. The anomaly definition mitigates problems associated with a short data record for TRMM-based events. For the longer GPCP record, departures from the linearly detrended calendar-day mean are used instead but compare favorably to anomalies as calculated in the appendix.

4. Results and discussion I: Composites of basic variables

The present study analyzes a host of nonprecipitation variables from the ERA-40 dataset. Several previous studies have suggested that analyses of synoptic and mesoscale tropical disturbances using nonprecipitation ECMWF reanalysis variables provide acceptable results. In their summary of meteorological results from Tropical Ocean Global Atmosphere Coupled Ocean–Atmosphere Response Experiment (TOGA COARE), Lin and Johnson (1996a,b) found that ocean–atmosphere evaporative fluxes and lower-tropospheric moisture values from the ECMWF reanalysis agreed relatively well with direct measurements from the TOGA COARE region. Straub and Kiladis (2003) analyzed convectively coupled Kelvin waves in the tropical west Pacific and found that, overall, the European Centre for Medium-Range Forecasts (ECMWF) reanalysis successfully depicted vertical structures of temperature, moisture, and zonal wind.

MJO events based on pentad- and meridionally averaged (10°S–5°N) TRMM precipitation are displayed in Fig. 2a. Of the 16 MJO events detected by the TRMM satellite, 11 are contained in ERA-40 and 13 in the MODIS dataset due to the partial overlap of the dataset time ranges. The locations of peak convection occur across a range of geographic regions, from the central Indian Ocean to the international date line. Events based on pentad- and meridionally averaged GPCP precipitation appear in Fig. 2b. There are a total of 46 GPCP-based events, each of which have corresponding ERA-40 fields. The TRMM- and GPCP-based events are well-distributed among the boreal nonsummer months, and there is essentially no dependence of event time on longitude.

The composite time–height plots for selected variables are presented in Figs. 3 and 4. Zonal wind cross sections (Fig. 3a) indicate the expected transition from surface easterly to westerly anomalies as the most intense rainfall propagates by (Madden and Julian 1972). Note that this surface wind transition occurs approximately four days before maximum total rainfall. The vertical velocity profile (Fig. 3b) suggests weak upward motion in the lower troposphere for about one week prior to the onset of deep convection near day −10.

The profile of specific humidity (q'; Fig. 3c) indicates that prior to intense convection, anomalously dry air is observed during the suppressed phase of the MJO throughout much of the troposphere. Beginning around day −20, there is a tendency for weak, shallow moistening to develop in the lower troposphere. Positive moisture anomalies deepen to approximately 500 hPa

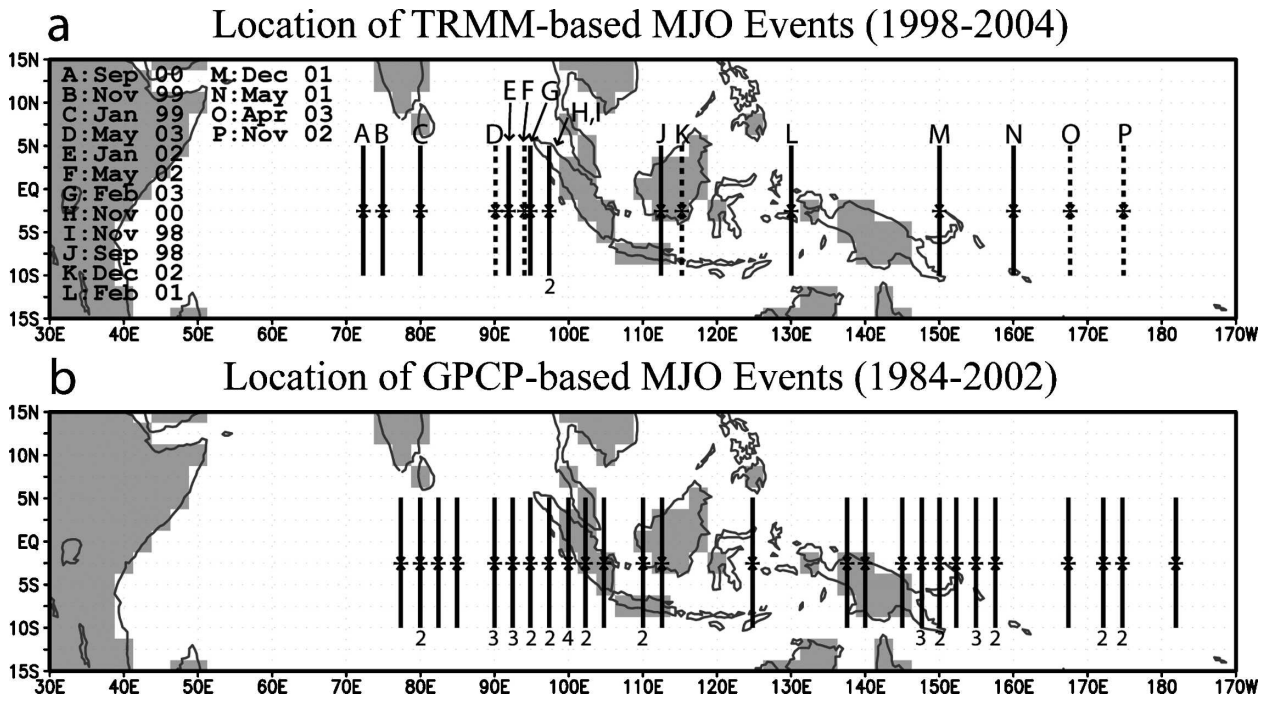

FIG. 2. (a) Map of MJO event locations, detected in both TRMM (solid and dashed) and ERA-40 (solid only) datasets that make up the TRMM-based composite plots. Vertical bars indicate that TRMM rainfall and ERA-40 data fields are averaged between 10°S and 5°N. Gray shading represents the ERA-40 land–sea mask. Numbers listed below the vertical lines indicate that more than one event occurred at that location. Letters above vertical lines correspond to event month and year listed at left. (b) As in (a), but for GPCP-based events. Events are evenly distributed among month and year and there is no dependence of event time on longitude, so no dates are listed for the 46 GPCP-based events.

between days −15 and −10. This progressive moistening coexists with weak rising motion (Fig. 3b) and convection (see section 5b). Maximum positive moisture anomalies appear on day 0 at the 600-hPa level. Drying ($\partial q'/\partial t < 0$) is first accomplished in the lower troposphere, beginning just before day 0 and expanding vertically upward with time. A slight decrease in relative humidity (not shown) accompanies this drop in q'. Most of the troposphere abruptly returns to the anomalously dry state by day +8. This structural evolution of the q' profile is consistent with the findings of many studies based on radiosonde data (Lin and Johnson 1996a; Kemball-Cook and Weare 2001; Straub and Kiladis 2003; KSH05) and remotely sensed vapor measurements (e.g., Myers and Waliser 2003).

Variations in temperature (T') are presented in Fig. 3d. At the time of maximum rainfall, much of the middle and upper troposphere is anomalously warm with a peak temperature perturbation of 0.7 K in the 300–400-hPa layer. Simultaneously, cool anomalies occur below 550 hPa and near the tropopause level. The composite structure of the lower-tropospheric cooling shown in Fig. 3d closely matches previous results based on radiosonde data (Lin and Johnson 1996a; Straub and Kiladis 2003; KSH05, their Fig. 8c), and probably arises from latent cooling of air within downdrafts (Reed and Recker 1971) and the evaporation of stratiform precipitation (Houze 1982). Between days −15 and −10, weak warm anomalies, a steady increase in low-level q', and the presence of shallow convection (see section 5b) support the view that shallow cumuli and their associated moistening and latent heat release play a role in preconditioning the atmosphere for later intense convection through destabilization (Kemball-Cook and Weare 2001; Straub and Kiladis 2003).

Time series of several pentad-averaged variables appear in Fig. 4. The anomalous surface latent heat flux (SLHF′) profiles in Fig. 4a indicate that for the composites based on TRMM rainfall (solid line, 11 total events), the most active latent energy exchanges between the atmosphere and ocean occur near day 0 with relatively weaker fluxes before and after intense rain. The composite profile of GPCP-based events (dashed line, 46 total events) suggests that the strongest surface latent energy fluxes are found between days 0 and +5, following maximum rainfall, an observation consistent with Jones and Weare (1996), Woolnough et al. (2000), and Sperber (2003). Owing to the extended data record

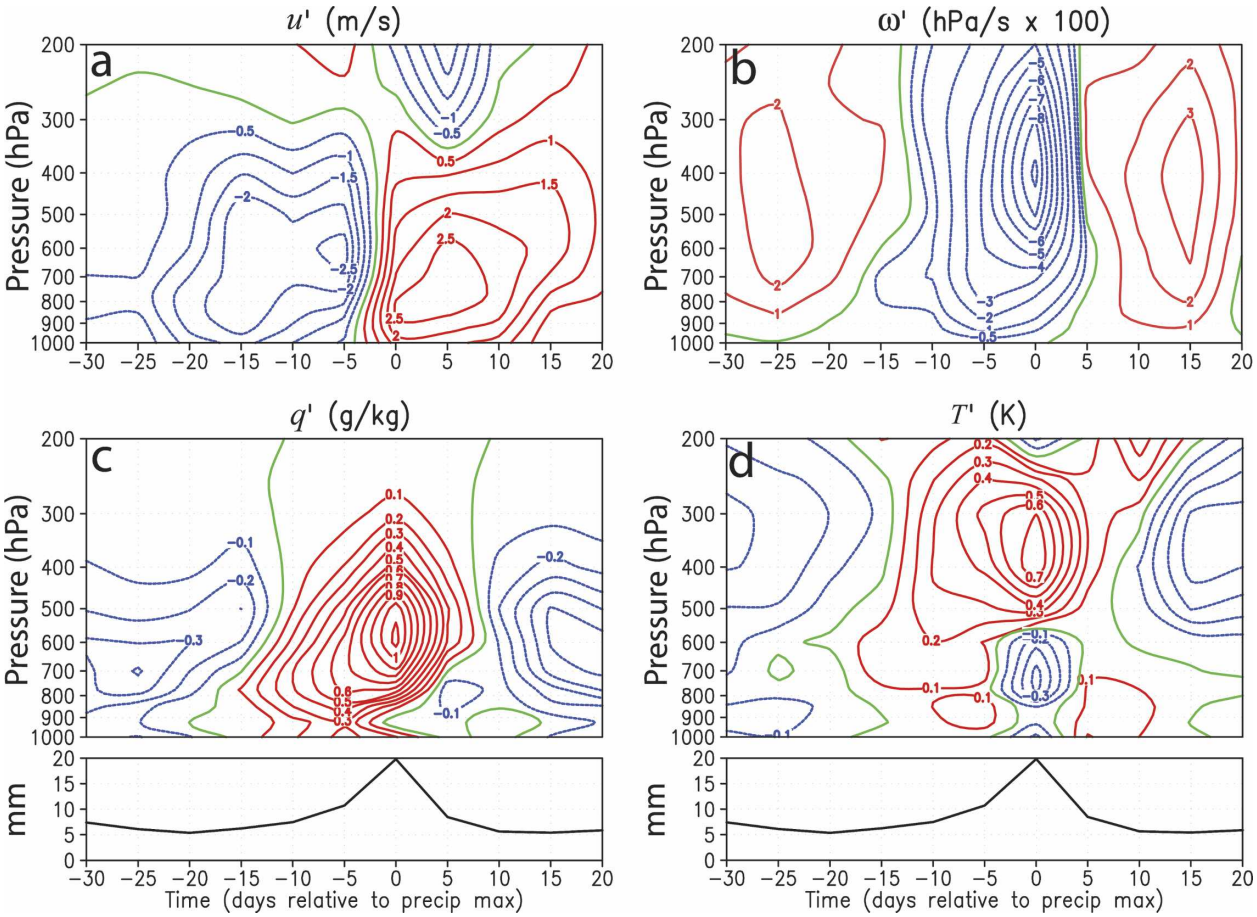

FIG. 3. Composite plots of pentad-mean (a) u', (b) ω', (c) q', and (d) T'. The corresponding composite TRMM rainfall time series appear below the lower panels. Solid red lines (dashed blue, solid green) are positive (negative, zero) departures from the MJO background state (see appendix). Lag days relative to maximum rain appear on the horizontal axis.

of the GPCP dataset, significance values are calculated and reveal that SLHF$' > 0$ for days 0, +5, and +15 are significant above the 95% level. Significance values are determined for GPCP-based events by comparing the anomaly value to a zero null hypothesis. Additional evidence based on daily averaged data (not shown) strongly indicates that wind-induced surface heat exchange (WISHE; Emanuel 1987) does not play a dominant role in the MJO composites. MODIS-derived CTP (Fig. 4b) and solar absorption at the surface (SSA′; Fig. 4c, dashed line) suggest a slight temporal asymmetry, with a gradual decrease in both variables prior to the wet phase followed by a more rapid return to the background state afterward. SST′ (Fig. 4c, solid line) generally rises between days −30 and −15 during which time SSA$' > 0$, suggesting less cloud coverage, weak ocean surface mixing, and minimal rainfall (Stephens et al. 2004). SST′ becomes increasingly negative as deeper convection develops and reaches a minimum near the time of the westerly wind burst (Lin and Johnson 1996a) about a week following maximum rainfall. Composite precipitable water perturbations (PW′, Fig. 4d) also display distinct temporal asymmetry relative to maximum rainfall: dry anomalies slowly erode toward a day-0 PW′ maximum, followed by a rapid return to below-average values. The time scale of gradual moistening prior to deep convection supports the discharge–recharge theory (Bladé and Hartmann 1993) and will be discussed in greater detail in section 6c.

5. Results and discussion II: MJO processes

In this section, we turn our attention to the advective and convective processes of the heat and moisture budgets associated with the MJO. These mechanisms represent the effect of large-scale components and the collective effect of small-scale components, including intrusions of drier air from the subtropics and shallow cumulus transports.

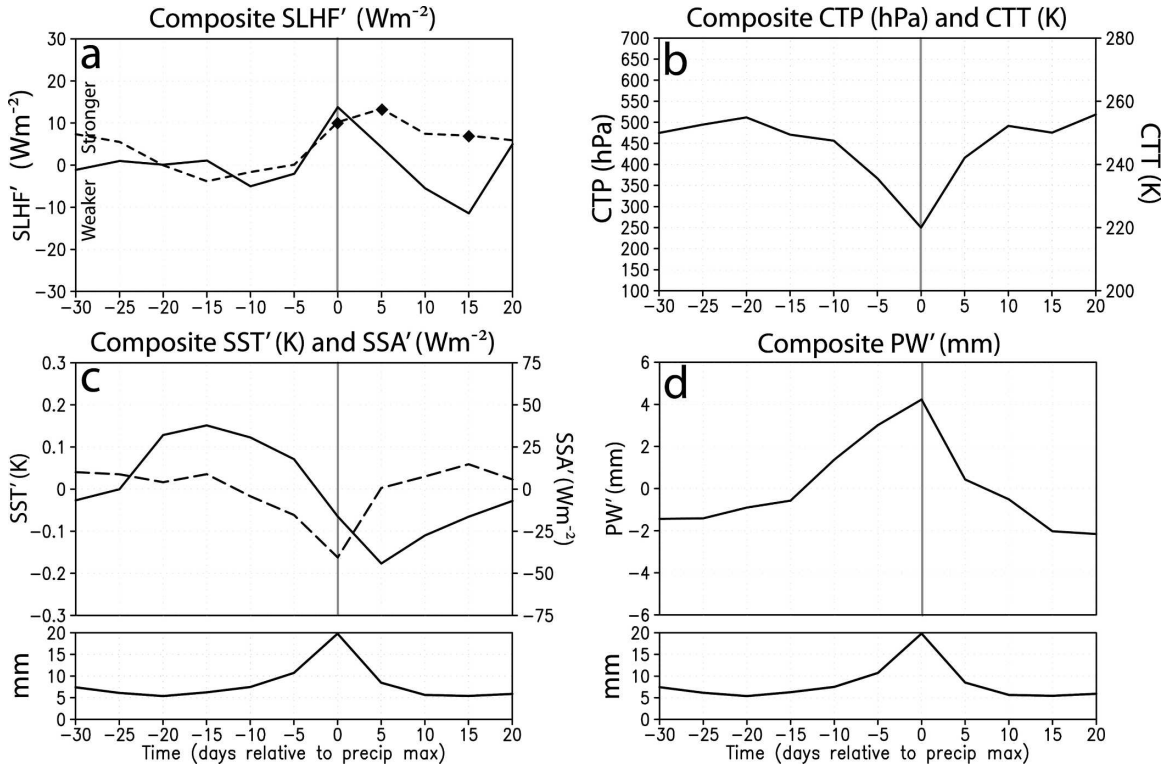

FIG. 4. (a) As is Fig. 3, but for ERA-40 anomalous surface latent heat fluxes for events based on TRMM precipitation (1998–2002; solid) and GPCP rainfall (1984–2002; dashed). For the GPCP-based composite, diamonds represent values greater than 95% significance. (b) MODIS CTP (left vertical axis) and CTT (right vertical axis), (c) ERA-40 SST′ (solid) and surface solar absorption (SSA′, dashed), and (d) ERA-40 precipitable water associated with TRMM-based events. Composited TRMM rainfall profiles appear below (c) and (d).

a. Horizontal and vertical components of advective moisture transport

Our first investigation, that involving advective processes associated with the MJO, addresses the specific humidity perturbation q'. A moisture-budget analysis is conducted by decomposing the local time rate of change of q' into its horizontal and vertical components:

$$\frac{\partial q'}{\partial t} = -\left(u\frac{\partial q}{\partial x}\right)' - \left(v\frac{\partial q}{\partial y}\right)' - \left(\omega\frac{\partial q}{\partial p}\right)' + S'_q - C'. \tag{1}$$

Here, S'_q and C' are the sources and sinks of q'. The contributions by S'_q and C' (evaporation and condensation, respectively) are not explicitly analyzed because of the absence of these ERA-40 data on individual pressure levels.

Figure 5 depicts the combined effects of the horizontal and vertical components that contribute toward changes in q' for all TRMM-based events (left column) and Indian Ocean (IO) GPCP-based events (right column). Indian Ocean events are those that occur between 50° and 100°E (see section 6a). Figure 5a displays the moderate, immediate drying brought about by the horizontal wind component between day 0 and +5. By comparison with Fig. 5c, it is clear that this horizontal drying component—associated with a reduction in q' (Fig. 3c) and relative humidity (not shown) with time—weakly counteracts the residual moistening tendencies of the vertical component, particularly during the first pentad following the peak of the wet phase at 600–800 hPa.

A more striking example of rapid drying is seen in Figs. 5b,d. Comparing the postconvective drying structure for these Indian Ocean events reveals that the horizontal and vertical components contributing toward $\partial q'/\partial t$ are comparable in magnitude and opposite in sign at 700–800 hPa on day +5. By day +10, the vertical drying component (subsidence) dominates over horizontal advection. This suggests that, especially for MJO events in the Indian Ocean, lower-tropospheric drying is first accomplished by westerly advection and later by subsidence as seen in Figs. 5b and 5d. Maloney

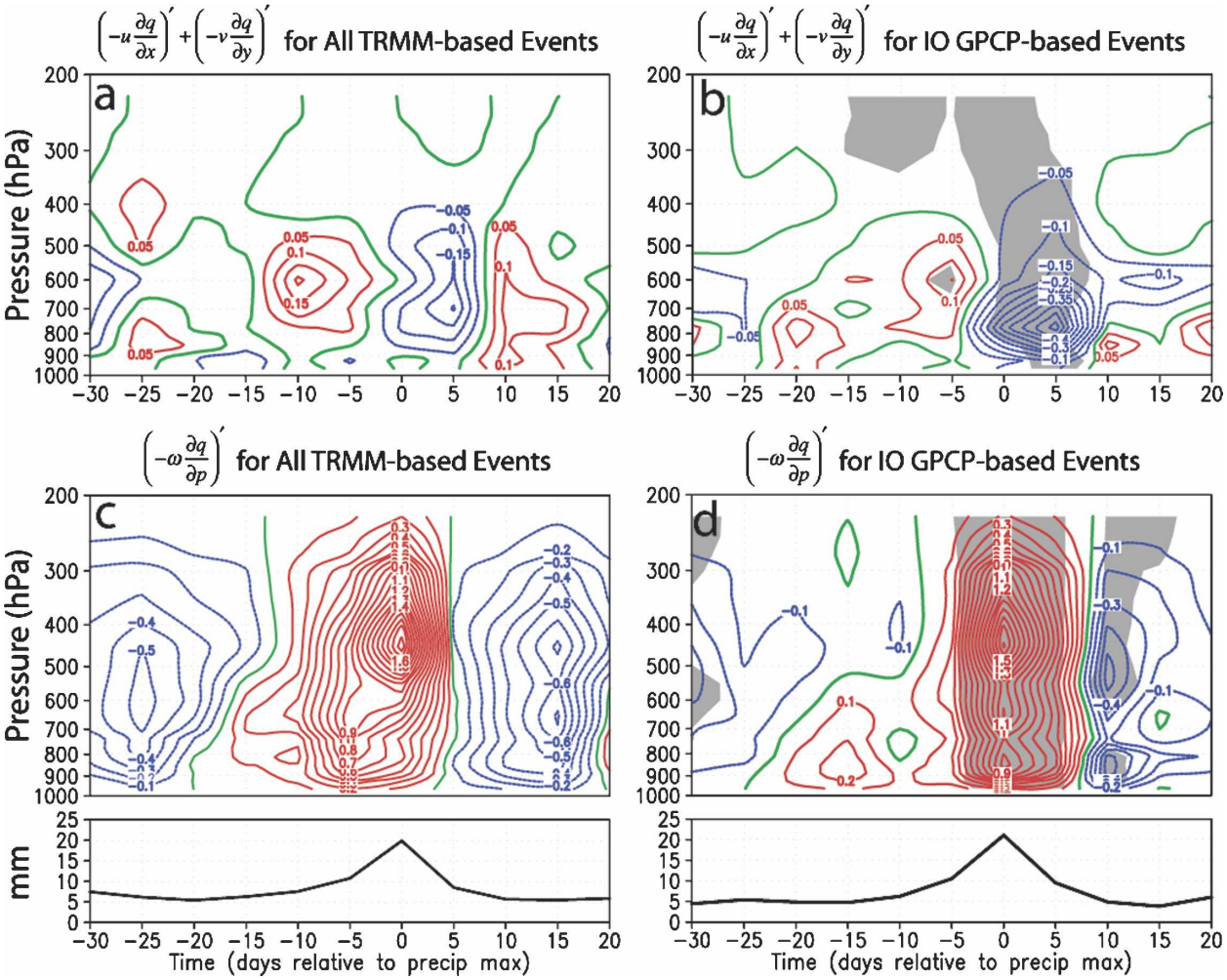

FIG. 5. (top) Composite plots of horizontal and (bottom) vertical components of the quantity $\partial q'/\partial t$ [(g kg^{-1}) day^{-1}]. (a), (c) Composites of all available events based on pentad TRMM rainfall; (b), (d) composites of Indian Ocean–only events based on pentad GPCP rainfall. (a), (c) Solid red lines (dashed blue, solid green) are positive (negative, zero) departures from the MJO background state (see appendix). (b), (d) For GPCP-based Indian Ocean events, departures are from the climatological calendar-day mean and 90% significance is indicated by gray shading. Note that for (a) and (b) contour intervals are half that of (c) and (d).

and Hartmann (1998) found that drying, particularly in the wake of MJO-like convective anomalies in the Indian Ocean, was associated with strong boundary layer divergence. It was speculated in their study that subsidence or horizontal advection may contribute toward this postconvective drying. The results in Figs. 5b and 5d illustrate that both of these mechanisms are active, and that subsidence drying follows horizontal advection in the case of Indian Ocean events. Postconvective drying by the horizontal wind component is far more substantial for GPCP-based Indian Ocean events when compared to the composite of all GPCP-based events. Moreover, composites of MJO events that occur between 100°–150°E (Maritime Continent) and 160°E–180° (west Pacific; not shown) reveal that the drying structures are geographically diverse, with weaker horizontal drying for Maritime Continent and west Pacific events as compared to those in the Indian Ocean. This raises the possibility that the strong horizontal drying seen in Indian Ocean events could partly be linked to their proximity to dry air mass origins, namely the arid regions of southwest Asia.

Postconvective drying can be parsed into immediate (horizontal) and delayed (vertical; subsidence) advective processes. Though noisier, composites formed from higher temporal resolution data (daily averaged, not shown) provide supporting evidence that substantial drying related to the horizontal winds can occur within the first pentad following intense rainfall. The concept of immediate and delayed drying mechanisms in the

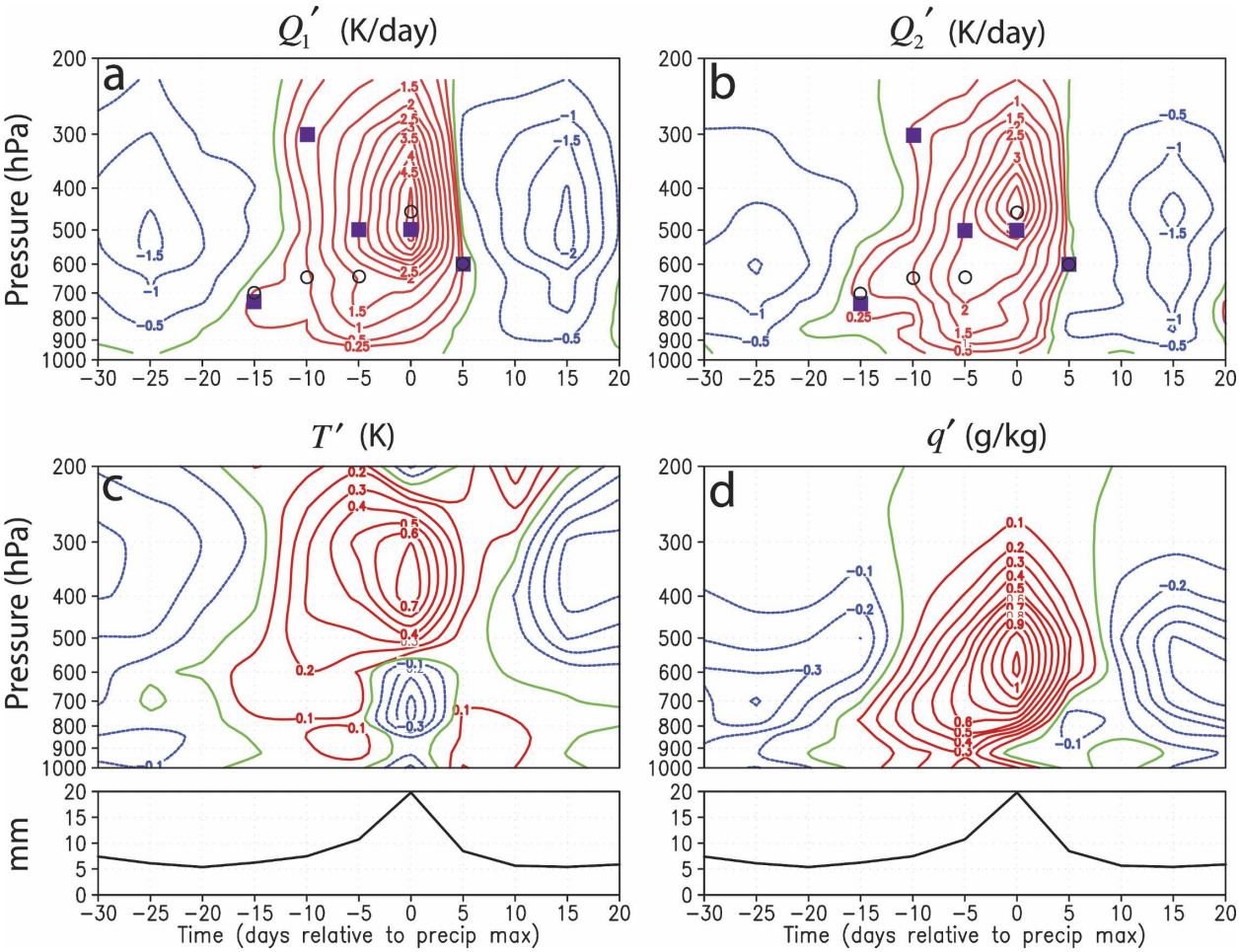

FIG. 6. Plots of (a) the apparent convective heat source Q_1', (b) apparent convective moisture sink Q_2' (positive values are associated with drying), (c) T', and (d) q' from the MJO background state (see appendix). The corresponding pentad-mean TRMM rainfall composites are reproduced at the bottom. The contour scheme is identical to Fig. 3 for T' and q'. In (a) the purple squares represent the height of maximum Q_1' for lag days −15 through +5, while open black circles depict the height of maximum Q_2'. These height values are reproduced in (b).

context of tropical waves has only recently been discussed in previous studies (Kemball-Cook and Weare 2001; Sperber 2003; KSH05). Maloney and Hartmann (1998) investigated postconvective drying processes associated with Rossby wave circulations emanating from MJO-related equatorial heat sources. Our results support their findings; that is, that drying is associated with strong lower-tropospheric westerly winds and boundary layer divergence about 10 days after the intense rainfall. We point out, however, that a more immediate drying component is seen in the reanalysis composites presented here, particularly for MJO events occurring in the Indian Ocean.

Rapid postconvective drying may be linked to the proximity of MJO events to dry air mass origins. A possible contributing factor to the immediate drying might also be midlevel westerly inflow below stratiform cloud decks of mesoscale tropical convective systems, as documented by Houze et al. (2000) during TOGA COARE in the west Pacific warm pool. Indeed, stratiform processes—as inferred by the temperature profile and vertical positioning of Q_1' and Q_2' maxima (see section 5b; Johnson and Young 1983; Luo and Yanai 1984)—appear to be active near the time of this drying in our results (see Figs. 6a,b,c). Houze et al. (2000) maintain that the exact nature of midlevel dry inflow hinges on the mutual interactions between mesoscale convection and the ambient dynamical fields (the forced Kelvin–Rossby wave response). Whether this interaction has a distinct longitudinal dependence in the Tropics remains unknown, but it is reasonable to expect that drying from the westerly midlevel inflow could be enhanced given a close proximity to dry air mass origins, as might be the case for events in the Indian Ocean.

In the weeks leading maximum total rainfall, moistening by the vertical wind component generally tends to outweigh moistening by the horizontal component, particularly between days −10 and 0. As will be shown in section 5b, low-level convective processes are active at this time, suggesting that the vertical moisture transport and lower-tropospheric heating are associated with shallow cumuli and cumulus congestus clouds.

b. Convective processes

We can infer that shallow convective processes are active prior to intense MJO rainfall by analyzing the apparent convective heat source (Q_1) and apparent convective moisture sink (Q_2) (Yanai et al. 1973):

$$Q_1 \equiv Q_R + L(c - e) - \frac{\partial}{\partial p}\overline{s'\omega'}$$
$$= c_p\left[\frac{\partial T}{\partial t} + \mathbf{v}_h \cdot \nabla_h T + \left(\frac{p}{p_o}\right)^k \omega \frac{\partial \theta}{\partial p}\right] \quad (2)$$

$$Q_2 \equiv L(c - e) + L\frac{\partial}{\partial p}\overline{q'\omega'}$$
$$= -L\left[\frac{\partial q}{\partial t} + \mathbf{v}_h \cdot \nabla_h q + \omega \frac{\partial q}{\partial p}\right]. \quad (3)$$

In (2), Q_1 is a combined measure of heating by radiation (Q_R), net latent heating [$L(c - e)$], and the vertical convergence of eddy sensible heat transports. In (3), Q_2 represents the net latent heating and the vertical convergence of eddy moisture transports. The magnitude of atmospheric heating or cooling brought about by convective processes can be deduced by measuring perturbations in the heat and moisture budgets applied on large (ERA-40 grid-box-sized) scales. If there are nonzero residuals computed from the large-scale budget analyses [rhs of (2) and (3)], these residuals represent the effects of subgrid-scale convection as applied to the larger gridbox area.

Time–height profiles of Q_1' and Q_2' (Fig. 6) indicate tropospheric cooling prior to day −20, probably due to radiation. The key feature occurs between days −15 and −5; at this time, positive T', q', and Q_1' exist between the boundary layer and about 600 hPa. Additionally, Q_2' shifts from moistening to drying between days −20 and −10, signifying a transition from lightly or nonprecipitating shallow clouds to deeper precipitating clouds. Together these observations indicate the presence and importance of deepening cumuli and the associated detrainment of moisture into the dry midtroposphere. Increased moisture in the mid- and upper-troposphere acts to decrease the efficiency of low-level radiative cooling and thus partially offsets cooling by upward motion. Using a simple atmospheric model, Bony and Emanuel (2005) show that, with a small convective time lag, the phase difference between heating and positive temperature anomalies in intraseasonal tropical disturbances decreases with stronger feedbacks between moisture and radiative cooling. Those authors maintain that feedbacks between radiation and enhanced moisture levels are vital in producing more realistic wave propagation speeds and growth rates for MJO-like disturbances.

c. Driving heat and moisture variances

Wave generation, amplification, and maintenance require an energy source. In the low latitudes, the generation of eddy available potential energy (EAPE) and its conversion to eddy kinetic energy (EKE) due to localized heating fuel tropical waves. EAPE is associated with heightened T variance and is increased when Q_1' and T' are the same sign. Vertical profiles of the product $Q_1'T'$ for three stages leading up to deep convection are displayed in Fig. 7.

Figure 7a represents averaged $Q_1'T'$ profiles (the average of the product) leading up to deep convection for all TRMM-based MJO events (see Fig. 2a). The first stage, an average between days −30 to −15 (dotted line), is generally associated with suppressed deep convection and $T' < 0$ and $q' < 0$ throughout much of the troposphere (see Fig. 6). The $Q_1'T'$ profile during this 15-day period suggests that radiative cooling dominates, especially above 500 hPa, acting to increase the temperature variance.

Between days −15 and −10 (dashed line, Fig. 7a), a weakly positive relationship between Q_1' and T' below 600 hPa reflects heating of anomalously warm air (see Fig. 6) by shallow convective processes, thus corresponding to EAPE generation. In light of Figs. 6 and 7, we can infer that there is likely an increase in the number and coverage of lower-tropospheric cumuli from days −15 to −10 as evidenced by the decline in surface solar absorption (SSA′; Fig. 4c), weak low-level rising motion (Fig. 3b), and $T' > 0$ and $q' > 0$ at low levels (Figs. 3d and 3c, respectively). Additionally, the positive relationship between Q_1' and T' above 500 hPa at this time likely displays the transition from radiative cooling of cool air to convective heating of warm air by emerging deep cumuli. Collectively, mid- and upper-level radiative cooling, elevated SSTs (Fig. 4c), and low-level heating and moistening effectively increase CAPE, thus destabilizing the atmosphere and preconditioning the region for an intensification of convection (e.g., Hu and Randall 1994; Kemball-Cook and Weare 2001). These features lend support to the discharge–recharge theory.

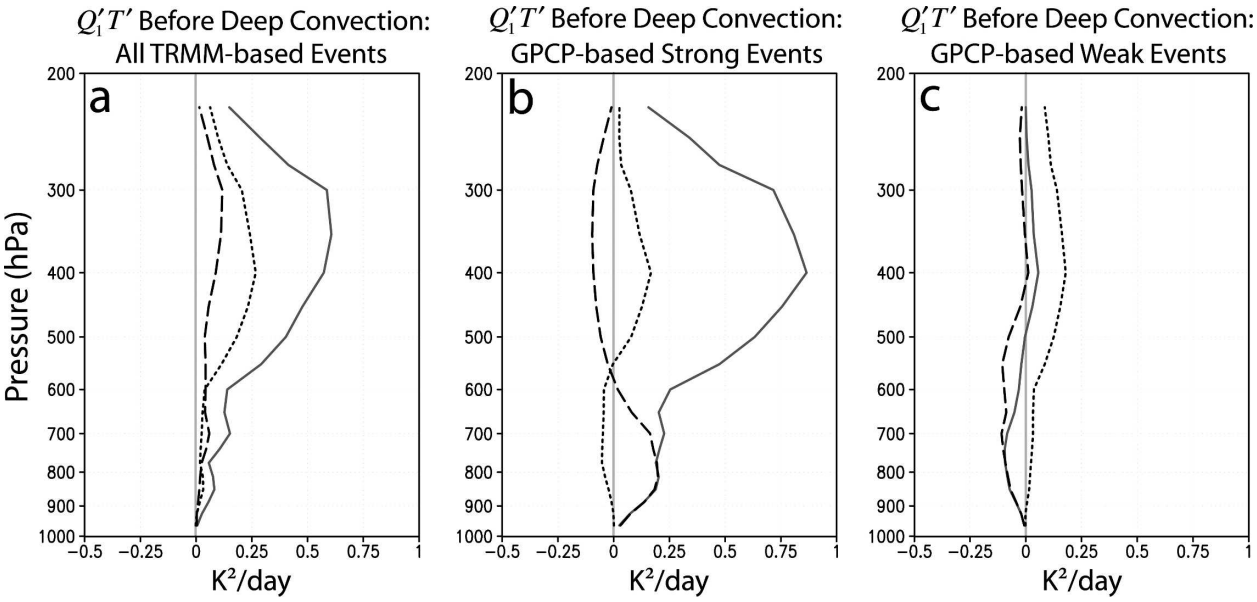

FIG. 7. Vertical profiles of $Q_1'T'$ for (a) all TRMM-based MJO events, (b) GPCP-based events associated with day-0 rainfall greater than $+0.75\sigma$ (strong events), and (c) GPCP-based events associated with day-0 rainfall less than -0.75σ (weak events). Individual profiles display the relationship between heating and temperature anomalies for three stages preceding deep convection. They are represented by dotted (days −30 to −20, inclusive), dashed (days −15 to −10, inclusive), and solid dark gray (days −10 to −5, inclusive) lines.

Increasing coverage, intensity, and vertical growth of cumuli occur between days −10 and −5 (solid dark gray line, Fig. 7a). Upward vertical motions and positive T' and q' (Fig. 4) rapidly extend toward the upper troposphere as deep convection becomes more active. Correspondingly, precipitation rates trend upward at this time. The deep convective heating, which dominates throughout the troposphere and corresponds to $T' > 0$ at all levels, effectively drives T variance and aids in EAPE generation leading to wave growth and the intensification of convective clouds.

Profiles of averaged $Q_1'T'$ (average of the product) during three stages preceding maximum precipitation for the strongest and weakest MJO events are displayed in Figs. 7b and 7c, respectively. A more detailed discussion of how these strong and weak events are selected can be found in section 6a. For the strongest MJO events, substantial convective heating of anomalously warm air below 600 hPa occurs between days −15 and −10 (dashed line in Fig. 7b), at which time cool anomalies exist in the mid- and upper troposphere (see Fig. 10). This setup results in an enhanced atmospheric destabilization and a more robust generation of EAPE as compared to Fig. 7a. For the weakest events (Fig. 7c), Q_1 works to decrease T variance in the lower troposphere between days −15 and −5 (dashed and solid gray lines), resulting in a destruction of EAPE. Further discussion of this topic will appear in section 6a.

6. Extended analyses and interpretation

Distinguishing characteristics of MJO events based on geographical location and relative event strength are highlighted in this section. Owing to the larger sample size, composites shown in Figs. 8–12 are based on GPCP rainfall. A discussion relating proposed wave instability theories and our results is included at the end of the section.

a. The MJO over an extended record: Geographical and strength distinctions

The composite fields for all 46 MJO events detected during the period of analysis (1984–2002) match up reasonably well with the composites based on pentad-mean TRMM rainfall (1998–2004). Because of the larger data sample, anomalies in this context are calculated as the departure from the linearly detrended, calendar-day means, and yield similar results to those generated from the calculations discussed in the appendix. Results from the GPCP-based composites support the findings in sections 4 and 5 and also provide an opportunity to examine differences in the MJO vertical–temporal structure based on geography and event strength.

Geographically, MJO events are subdivided by region: Indian Ocean (50°–100°E; 15 events), Maritime Continent (MC; 100°–145°E; 14 events), TOGA

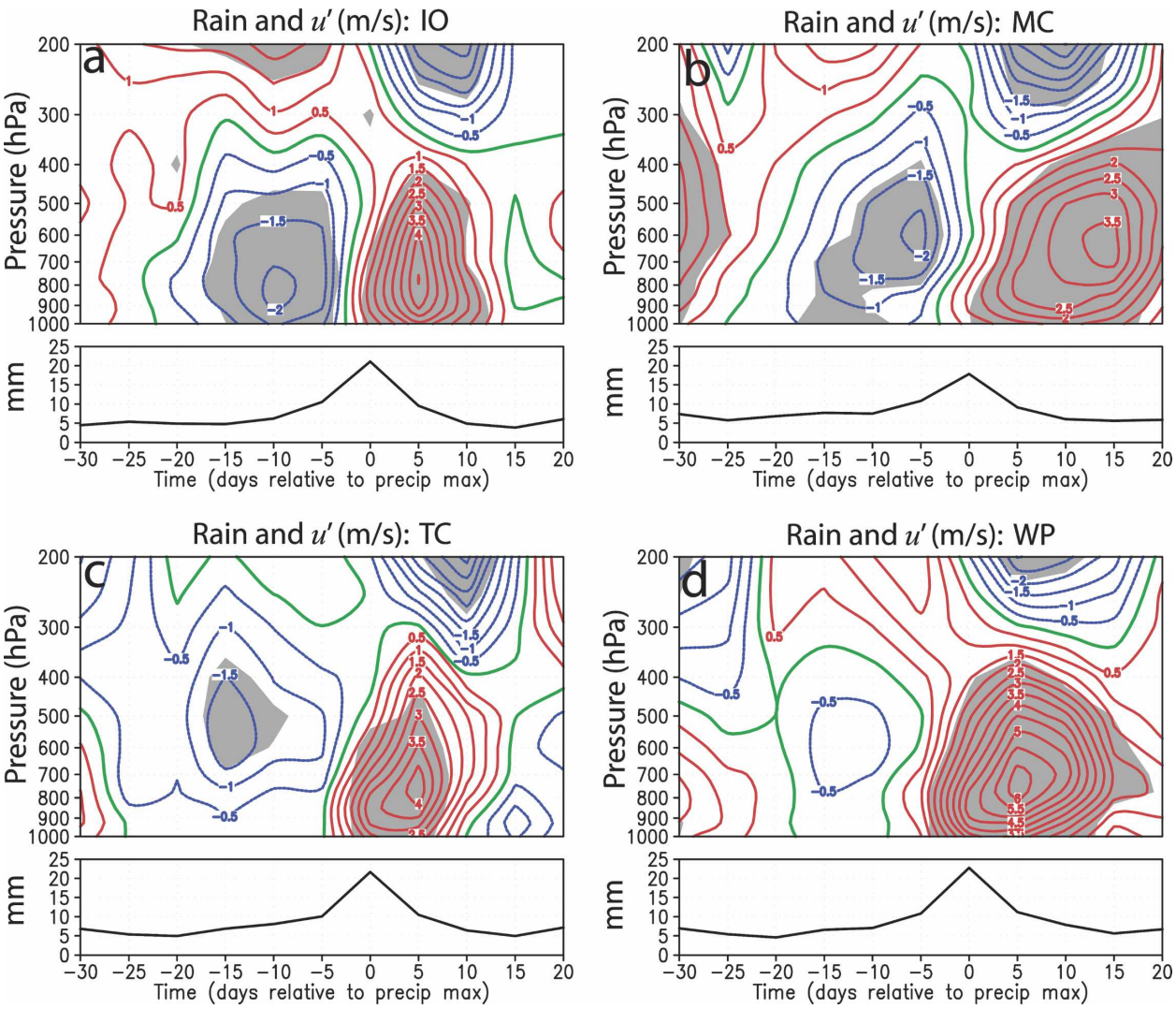

FIG. 8. Composite plots of u' for GPCP-based MJO events in the (a) IO, (b) MC, (c) TC, and (d) WP regions. Corresponding GPCP precipitation profiles appear below each panel. Solid red lines (dashed blue, solid green) are positive (negative, 0) departures from climatological calendar-day means (1984–2002). Gray shading represents significance values greater than 90%.

COARE (TC; 150°–160°E; 8 events), and west Pacific (WP; 145°–180°E; 17 events). WP events, as measured by maximum day-0 rainfall, tend to be more intense than those in other regions. The composites suggest that the suppressed phase of the MJO is most notable in the IO, where comparatively low rain amounts are observed when deep convection is inactive. The range of rainfall amounts is least for MC events, likely due to land surface heating and diurnal convection even during the suppressed phase.

Cross sections of u' (Fig. 8) indicate that wind structures in the IO are more vertically stacked than in regions farther east. Low-level easterly anomalies prior to deep convection tend to be stronger in the IO as well, with a notably weaker signal for WP events. Aside from the pronounced westward vertical tilt, the u' westerly maximum for MC events is delayed by two pentads and is higher (650 hPa) when compared to IO and WP events, which have a day +5 peak at 750 hPa. This u' delay and upward shift, as well as several other general features of the vertical–temporal structure, are qualitatively similar to those found in previous studies (e.g., KSH05).

Plots of T' for the MJO regional analysis (not shown) provide an interesting comparison with the results of KSH05. Our results for the MC case closely match the T' structure at Medan (KSH05, their Fig. 8c), a west Indonesian island location, where cool anomalies below 800 hPa and above 600 hPa with a warm layer in between precede deep convection. In contrast, WP events

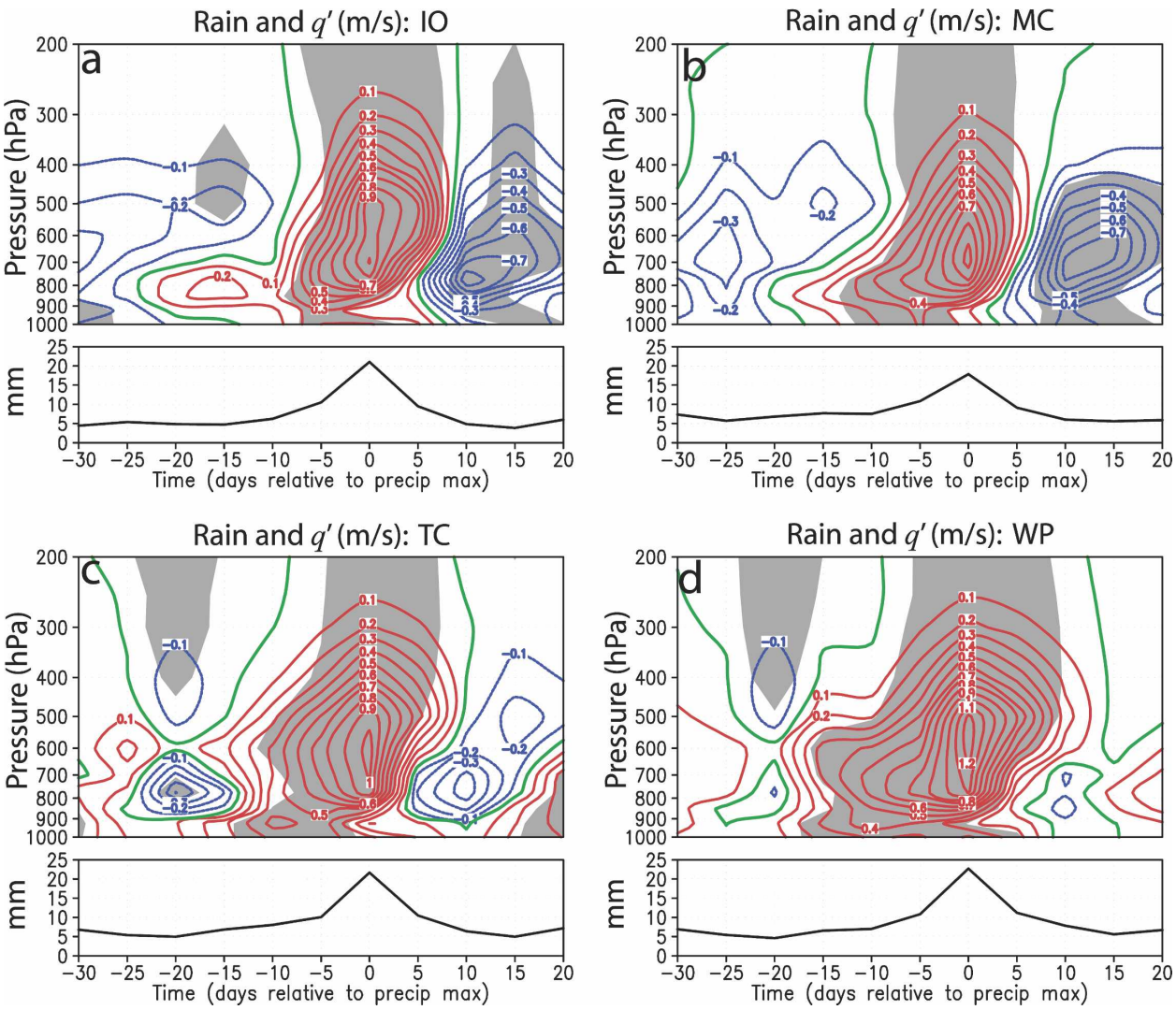

FIG. 9. As in Fig. 8, but for q'.

display a more extended period of warm anomalies throughout the sub-600-hPa level prior to intense rainfall, consistent with KSH05 and indicative of a gradual vertical progression of warmth (and moisture) into the middle and upper levels as deeper convective clouds develop.

Moisture profiles (Fig. 9) reveal several geographic differences. Composites of ERA-40 q' for IO events display a prolonged period (day -25 to -10) of marginally positive values below 750 hPa with dry anomalies aloft, followed by an abrupt and significant deepening of moisture into the midtroposphere after day -10. MC events are associated with a more gradual rise in q' with time. Moisture profiles from the TC region (Fig. 9c) are similar to WP events and depict the development of a $q' > 0$ tongue near the surface on day -20, which then evolves into a deeper layer of positive anomalies. Overall, a more robust signal of prolonged, positive low-level moisture anomalies prior to deep convection is seen in WP events compared to those farther west (MC, IO). These results are generally consistent with radiosonde-based findings of Straub and Kiladis (2003) and KSH05, with the exception of the earlier appearance of the shallow moist layer for IO events (Fig. 9a). We ascribe this difference to the fact that most IO events are located in the central or eastern IO and thus potentially share more similarities with MC events than the selected q profile at Diego Garcia (KSH05, their Fig. 10a), which is in the western IO.

In addition to geographical differences, MJO events are also categorized into strong and weak events based on day-0 rainfall. Strong (weak) events are defined as

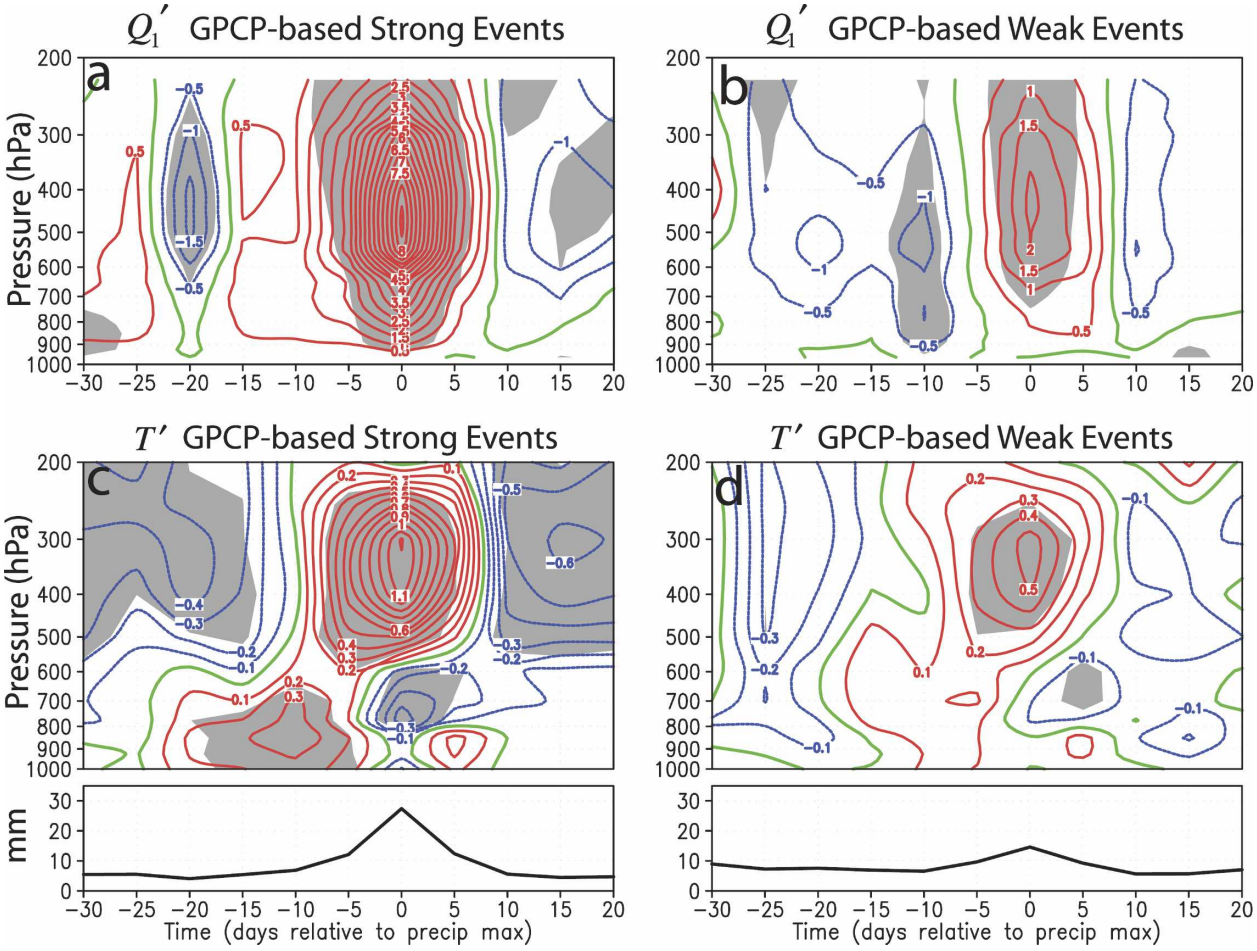

FIG. 10. Plots of the (top) apparent convective heat source Q_1' and (bottom) temperature T' for MJO events based on GPCP rainfall. Plots for the strongest (weakest) events appear in the left (right) column. The corresponding rainfall composites are reproduced at the bottom. The contour scheme is similar to Fig. 6. Gray shading represents significance values greater than 90%.

those in which day-0 rainfall is 0.75σ greater (less) than the mean day-0 rainfall of all events. Of the 46 total events, 10 are classified as strong and 11 weak. This categorization of event strength might provide some insight into what features are prominent during vigorous MJO activity. It is well known that many current atmospheric GCMs lack a realistic MJO-related variance for many fields, including T' and q' (see review in Lin et al. 2006). Thus, analyzing the observed behavior of such variables before and after MJO events and comparing this behavior to GCM output might aid in understanding model deficiencies.

Concerning T' (Figs. 10c,d), strong events have more pronounced and extended lower-tropospheric warm anomalies preceding intense MJO-related rainfall. This warmth is confined to below 700 hPa while abnormally cooler air exists above 600 hPa prior to day −10, indicative of a more unstable atmosphere for the strongest events. This temperature structure qualitatively resembles that found by Lin et al. (2005) who used ERA-15 data, although those authors did not distinguish vigorous and weak MJO events. Weaker events have only marginal warm anomalies, which are positioned at a higher level (550–750 hPa) and develop one pentad after those seen in the strong event composite. As tropical atmospheric warming is intimately related to cloud and radiative processes (e.g., Reed and Recker 1971; Cox and Griffith 1979), it is likely that the contrasting behavior in T' structure between weak and robust MJO events is directly linked to cumulus activity.

Profiles of q'(Fig. 11) suggest that increased levels of lower-tropospheric moisture develop earlier and are deeper for strong MJO events. The onset of $q' > 0$ for strong events (Fig. 11a) occurs near 900 hPa and day −20, followed by a secondary lobe of development at 550–700 hPa on day −15 and then gradual deepening. In weaker events (Fig. 11b), low-level moisture increases first at 850 hPa near day −15 (one pentad later

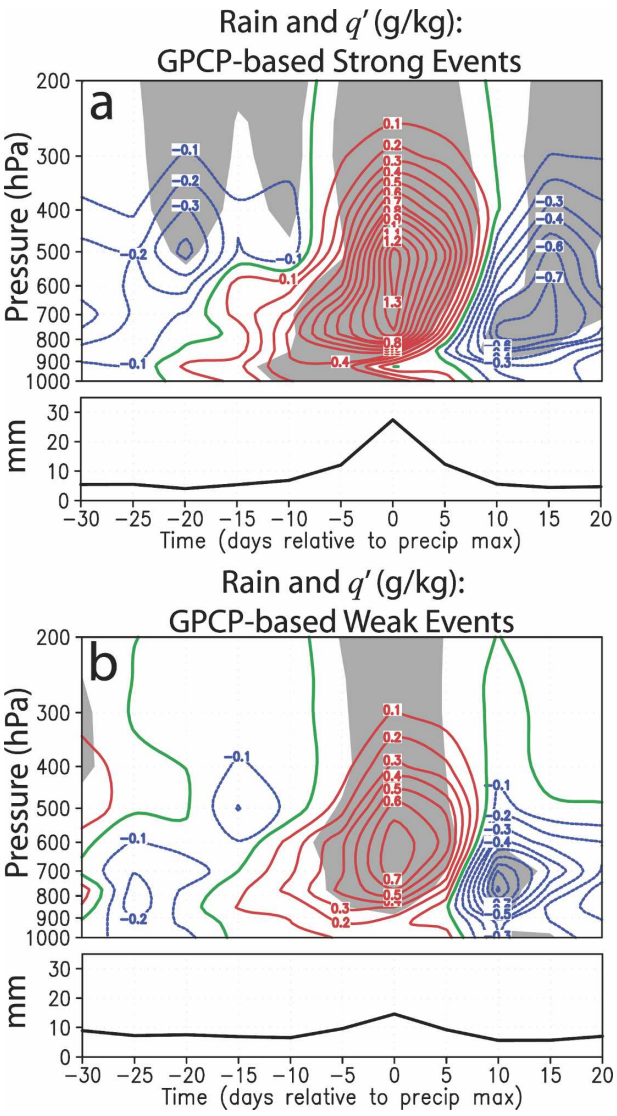

FIG. 11. As in Fig. 10, but for q'.

than strong events) and then gradually deepens. The structural differences between the onset of $q' > 0$ seen in Fig. 11 may play an important role in differentiating fundamental physical processes that govern generation and maintenance of MJO-related convection. The authors hypothesize that the two-tiered signal of q' may reflect the position of stable layers [the trade inversion near 850 hPa and the freezing level near 550 hPa (Johnson et al. 1996; Kikuchi and Takayabu 2004)]. It is possible that the presence of these layers allows moisture to accumulate below them, thus leading to more sudden and vigorous convection and diabatic heating several days afterward. No such tiered structure exists in the weak-event composite. What role stable layers might play in MJO events, and exactly how these layers influence or are influenced by the events themselves, remains an intriguing question.

One of the most striking contrasts between strong and weak MJO events is a lack of convective heating prior to maximum precipitation for weak events (Figs. 10a and 10b), as discussed in section 5c with reference to Figs. 7b and 7c. Figure 10a, the composite of vigorous MJO events, indicates that convective processes are active two weeks before the most intense rainfall is observed. Around this time, warm and moist anomalies (Figs. 10c and 11a, respectively) coexist with lower-tropospheric convective heating, as do distinct upward velocity perturbations and anomalous upward moisture transport (not shown). This likely signifies the presence of shallow cumuli and cumulus congestus clouds. We can infer from Fig. 10b that cumulus activity in weak events is far more isolated and does not precondition the atmosphere as efficiently. These results illustrate the importance of relationships between lower-tropospheric heating and moistening, the degree of EAPE generation, and the extent of atmospheric destabilization prior to the onset of robust MJO-related deep convection. Additionally, Fig. 10 reiterates the need for GCMs to accurately parameterize or explicitly simulate shallow cumuli and their effects on the neighboring environment in relation to the MJO.

b. *A note on statistical significance*

As a brief digression, we examine issues of statistical significance. Owing to its short data record, we did not display statistical significance values for the composites based on TRMM precipitation. However, significance values for all GPCP composites were calculated, and values greater than 90% (based on a zero null hypothesis) appear as gray shading in the appropriate figures. Despite the limitations of the TRMM data, we feel that the results are physically meaningful. For example, although significance is below 95% in the lower troposphere between days -15 and -10 in the plot of Q_1' (Fig. 6a), active vertical moisture transport and warm, moist anomalies (Figs. 6c and 3) suggest a physical link explained by shallow convective clouds. Additionally, observational experiments such as TOGA COARE testify to the presence and importance of such shallow cloud activity (Lin and Johnson 1996b; DeMott and Rutledge 1998).

c. *Wave theories and the MJO: Interpreting the results*

Over the past three decades, several theories have been proposed detailing the physical mechanisms that generate and maintain the MJO. Versions of these

theories fall into several categories: 1) wave-CISK, 2) WISHE, 3) stratiform instability, 4) frictional–convergence feedback, and 5) the discharge–recharge mechanism. In this section, we review the results of this study to determine the degree of consistency between each proposed theory and the observations.

Wave-CISK involves instability that occurs as a result of cooperation between localized convective heating and its environmental large-scale circulation (e.g., Hayashi 1970; Lindzen 1974). An important aspect of wave-CISK is a positive correlation between deep convective heating and positive temperature anomalies. In vigorous (weak) convective regions, the Q_1 and Q_2 peaks are well-separated (nearly collocated) in the vertical (e.g., Johnson and Young 1983). In Figs. 6a and 6b, plots showing the peak heights of Q_1' (purple squares) and Q_2' (open circles) give some indication of where vigorous deep convection is likely occurring. Possible evidence of wave-CISK-like processes is noted in the observation that initial deep convection (see Fig. 6a) and its associated first-mode heating occur simultaneously with deep warm anomalies between days −10 and −5. Additionally, this deep convective heating lags 600–800 hPa T' maxima by about 7–10 days [out of phase by >0.25 cycles as in Straub and Kiladis (2003)]. It is possible that, between days −15 and −10, the inferred shallow cumuli partake in a CISK-like process in which shallow heating generates weak low-level moisture convergence (Wu 2003) prior to MJO-related deep convection. Figure 6 indicates that on day 0 a strong positive (negative) correlation between heating and temperature is observed above (below) 550 hPa. The destruction of EAPE in the lower troposphere suggests that wave-CISK-like processes are becoming less pronounced and that other instability mechanisms may be emerging. In general, instability mechanisms related to wave-CISK appear to be active during the two weeks preceding day 0 in the composites shown. However, several studies (e.g., Lau and Peng 1987; Wang 1988; Matthews and Lander 1999) have highlighted inconsistencies between theory and observations, indicating that a direct application of the traditional wave-CISK theory does not fully explain the observed disturbance.

The WISHE mechanism (e.g., Emanuel 1987) involves an instability that arises through the interaction of surface latent heat fluxes and large-scale wave dynamics. The results of this study suggest that the WISHE mechanism is not a critical component in the events examined. In general, we found that surface fluxes are stronger in the wake of the disturbance, supporting the results of many other studies (e.g., Jones and Weare 1996). To examine possible geographic differences of the phase relationships between SLHF′ and maximum rainfall, we present Fig. 12. From this figure, it is apparent that a stronger SLHF occurs within the first pentad following the disturbance for both Indian Ocean and west Pacific events but not those near the Maritime Continent (dot–dashed line). West Pacific events have a more robust phase relationship between SLHF′, maximum rainfall, and maximum surface westerlies (Fig. 8) when compared to Indian Ocean events, consistent with the findings of Zhang and McPhaden (2000).

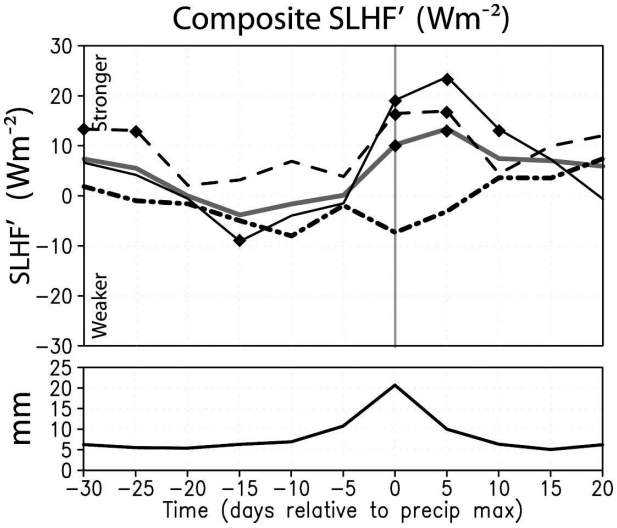

FIG. 12. Composited ERA-40 anomalous surface latent heat fluxes for MJO events occurring in the Indian Ocean (dashed black), Maritime Continent (dash–dot black), west Pacific (solid black), and all events (thick solid gray). Diamonds represent values greater than 95% significance. Events are based on pentad- and meridionally averaged (10°S–5°N) GPCP rainfall. Corresponding mean rainfall profile appears in the lower panel.

Stratiform instability arises from a positive correlation between a second-mode temperature profile and second-mode stratiform heating structure (Houze 1997; Mapes 2000). Our results suggest that the stratiform instability mechanism likely plays an important role a few days before and after maximum rainfall, when stratiform processes appear to be most active (Fig. 3d). Perhaps this mechanism prolongs convection and the MJO wet phase itself by reducing convective inhibition (CIN) and regenerating or maintaining residual convection, particularly during the first pentad following maximum rain intensity. For example, a top-heavy heating profile for the composite of strong MJO events (Q_1'; Fig. 10) is observed between days 0 and +5 when the temperature profile is stratiform. At this time, some evidence of a secondary maximum of Q_2' (not shown) occurs in the lower troposphere and is well-separated from the Q_1' peak aloft, suggesting that scattered residual deep convection may be present. However, the

precise character of convective intensity is difficult to assess, especially in the days following maximum rainfall, and no such separation of Q_1' and Q_2' peaks is observed for the composite of all TRMM-based MJO events (Fig. 6). Stratiform instability theory accurately depicts several aspects of MJO-like disturbances but alone cannot effectively explain the entire life cycle. Model simulations of disturbances generated by stratiform instability (see Mapes 2000) display several inconsistencies with observations, including warm-over-cold anomalies leading intense convection and disturbance propagation speeds of about 20 m s^{-1}. Observations indicate that MJO-like disturbances propagate at less than 10 m s^{-1} (Weickmann et al. 1985) and that upper-tropospheric warm anomalies are collocated with convective heating (Q_1'; Fig. 6).

The MJO involves various interactions, those between different spatial scales, between temporal scales, and between the ocean, boundary layer, and free atmosphere. Concerning the latter, a critical component of the observed MJO is the variability of water vapor in the lower troposphere. An important factor contributing to the fluctuations in low-level moisture is the sign and magnitude of friction-induced divergence within the boundary layer, a central concept of the frictional-convergence theory (e.g., Wang 1988; Salby et al. 1994; Maloney and Hartmann 1998). For near-equatorial, planetary-scale heating regions, a Kelvin wave response to the east of the heating produces anomalous low-level easterly winds. Above the boundary layer, geostrophic dynamics dominate; within the boundary layer, geostrophy breaks down due to frictional influences, allowing easterly winds to converge and water vapor to accumulate. Our results generally lend support to frictional-convergence theory. An analysis of composite ERA-40 1000-hPa winds shows that near-surface flow is convergent (divergent) prior to (after) the onset of heaviest rainfall associated with the MJO (not shown). Low-level vapor anomalies are positive and increasing between days −15 and −5 (Fig. 3c), coincident with the boundary layer convergence. Although frictional-convergence theory selects appropriate spatial scales for MJO-related disturbances (Wang 1988), its role in explaining the dynamical connection between successive initiations of MJO disturbances in the west central Indian Ocean is not well understood (Sperber 2003).

Another school of thought involving the origin of the MJO centers on a local, gradual buildup of instability through low-level warming and moistening and radiative cooling aloft that preconditions the atmosphere for episodes of deep convection associated with the MJO. This process—the discharge–recharge mechanism (Bladé and Hartmann 1993)—maintains that globally circumnavigating Kelvin wave signals are not necessary for reinitiation of MJO-like convection in the west central Indian Ocean, but rather extratropical stochastic forcing applied to a primed atmosphere can ignite MJO disturbances.

The results of the present study compare favorably with theories of gradual enhancement of instability and cumulus growth, as outlined in such papers as Bladé and Hartmann (1993), Hu and Randall (1994), and Kemball-Cook and Weare (2001). For example, time–height cross sections of ω', T', q' (Fig. 3), and Q_1' (Fig. 6) as well as profiles of CTP, SSA′, PW′ (Fig. 4), and OLR′ (not shown) clearly suggest a slow buildup of low-level warming, moistening, and cumulus growth. Relative to the maximum total rainfall, there is an asymmetry in time scales of the recharge and discharge phases (e.g., PW′ in Fig. 4), such that convective dissipation and tropospheric drying occur more rapidly than cumulus growth and tropospheric moistening. Temporal asymmetries associated with MJO-related convection have also been proposed in previous studies (e.g., Maloney and Hartmann 1998; Stephens et al. 2004). In Fig. 13, a schematic diagram of the discharge–recharge mechanism as seen in the reanalysis data is presented. In terms of q' and T' (Figs. 3c and 3d), for instance, low-level warming and moistening are maximized for ~10–15 days, deep convection and precipitation processes ultimately serving to stabilize the troposphere are active for ~10 days, and suppressed convection with associated tropospheric drying are observed for ~20 days, thus yielding a 40–45-day oscillation. The time scales of these MJO stages might involve links between the hydrologic cycle and the ocean surface in addition to the atmospheric component as in Bladé and Hartmann (1993). For example, Stephens et al. (2004) related the mutual interactions between intraseasonal variations in SST′ with fluctuations in rainfall intensity, SSA′, and SLHF′ caused by the MJO.

Evidence in support of localized destabilization via low-level warming and moistening is seen in the dominance of anomalous vertical moisture transport over horizontal transport (Figs. 5a and 5c) ~5–15 days prior to maximum rainfall. Although the $(-\omega\partial q/\partial p)'$ term strictly represents anomalous vertical advection of water vapor on the mesoscale (or larger), convective processes are active at this time (Fig. 6a) and their collective contributions presumably influence the low-level temperature and moisture fields above the boundary layer. It is likely that frictional moisture convergence within the boundary layer and modest evaporative fluxes promote shallow cumuli and later cumulus congestus that ultimately warm and moisten the lower free troposphere and destabilize the atmosphere, paving the

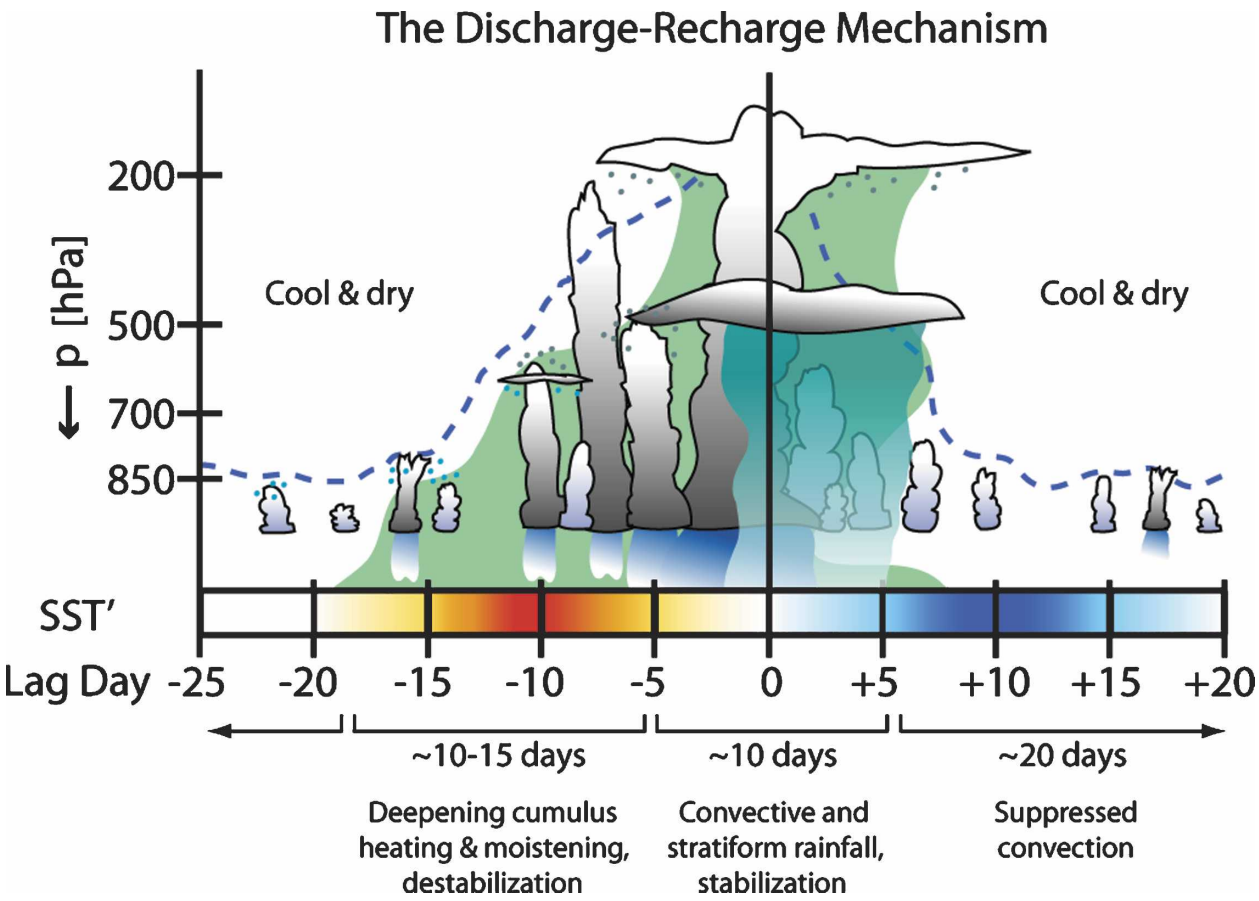

FIG. 13. Schematic diagram of the discharge–recharge mechanism associated with the MJO. Along the horizontal axis appears SST′ [red (blue) indicates warmest (coolest) anomalies] and the lag days relative to the day of maximum rainfall (day 0). Stages of the discharge–recharge process, as seen in ERA-40 data, are listed below the lag days. The approximate top level of convective cloud processes is indicated by the dashed blue line, while green shading represents the general area of $q' > 0$. Light blue dots above shallower convective clouds represent moistening via detrainment, while gray dots below stratiform cloud types represent ice crystal fallout and moistening. Convective precipitation is indicated by darker blue rain shafts, and stratiform precipitation is light blue and slightly transparent.

way for deep convection. For most of the events in the composites presented, the buildup of low-level heat and moisture is accomplished more by localized mechanisms rather than by large-scale advective processes.

A final aspect of the discharge–recharge theory concerns the geographical characteristics of the MJO events analyzed and their related triggering mechanisms. In this study, most of the individual events are located in the eastern Indian and western Pacific Ocean areas (Fig. 2). We chose these locations to correspond to maximum wet phase amplitude and not wave initiation, and so it is likely that the composite results largely reflect the evolution of a (nearly) fully developed convective envelope. Inspection of the total-event composite of daily averaged dry static stability [$\hat{\theta}' = \frac{1}{2}(\theta'_{250\text{hPa}} - \theta'_{775\text{hPa}})$; Fig. 14] supports this hypothesis, showing the shape of the $\hat{\theta}'$ profile to be similar to a model-generated stability composite of events 90° downstream of wave initiation (Fig. 11c in Bladé and Hartmann 1993). Overall, the theory that involves a local, gradual buildup of low-level heat and moisture acting to destabilize the atmosphere (e.g., discharge–recharge mechanism) successfully explains many of the observed features of MJO evolution.

d. Synthesizing wave theories and observations

A comparison of the observational results in this paper with the proposed wave instability theories reveals that specific processes are more important during certain phases of the MJO. Prior to the most intense rainfall, gradual atmospheric destabilization develops and is related to enhanced surface solar absorption and warming at low levels and radiative cooling aloft (e.g., Hu and Randall 1994; Stephens et al. 2004). As easterly

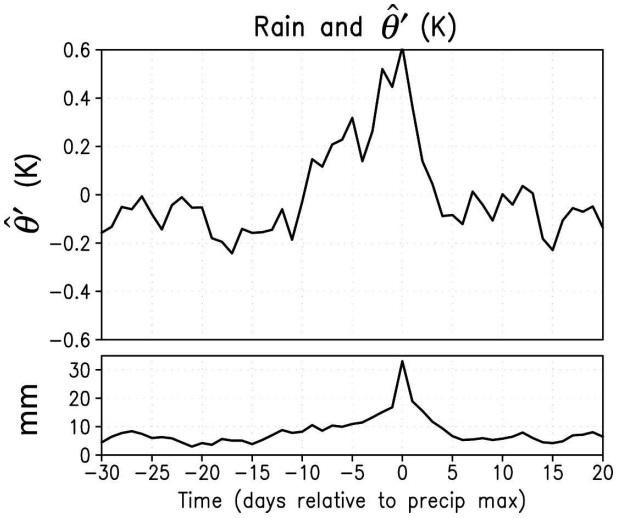

FIG. 14. Time series of the composited departure of daily averaged dry static stability [$\hat{\theta}' = \frac{1}{2}(\theta'_{250\text{hPa}} - \theta'_{775\text{hPa}})$] from climatological calendar-day means (1984–2002). The composite time series of daily averaged TRMM precipitation appears in the lower panel.

low-level wind anomalies develop about 2–3 weeks before the onset of deep convection, the accumulation of moisture in the boundary layer—perhaps by frictional convergence or modest evaporative fluxes—promotes shallow cumuli and later cumulus congestus growth that ultimately warms and moistens the lower free troposphere (e.g., Bladé and Hartmann 1993; Hu and Randall 1994; Maloney and Hartmann 1998). While these discharge–recharge and frictional-convergence mechanisms operate, wave-CISK-like processes begin to emerge. Shallow cumuli and cumulus congestus possibly induced by larger-scale wave dynamics and frictional moisture convergence generate secondary circulations that reinforce low-level moisture convergence (Wu 2003).

Deep convection begins to develop about 7–10 days prior to maximum total rainfall and is associated with a positive relationship between first-mode heating and tropospheric temperature anomalies, as outlined by traditional wave-CISK theory (e.g., Hayashi 1970). This positive relationship between heating and temperature anomalies generates EAPE and promotes wave growth. Additionally, the contributions of friction-induced boundary layer moisture convergence (Wang 1988) and moisture–radiation feedbacks (Bony and Emanuel 2005) work to ensure that the disturbance selectively develops on planetary scales and propagates at speeds mandated by convective coupling.

Near the time of the greatest total rain intensity, deep heating from vigorous convection begins to evolve into second-mode stratiform heating, signaling the emergence of the stratiform instability mechanism. Negative temperature anomalies develop below the tropical freezing level (~550 hPa) and reduce CIN. The reduction in CIN could foster residual convection, consistent with the stratiform instability mechanism (Mapes 2000), and prolong the MJO wet phase by several days.

Within the first week following maximum total precipitation, low-level drying accomplished primarily by horizontal advective processes is observed (Fig. 5; see also Maloney and Hartmann 1998). Drying associated with deep subsidence begins to develop by the end of the first week and reaches a maximum intensity approximately 10–15 days following the peak of total rain. Deep convection, which is partly linked to the degree of moist static energy in the boundary layer, is suppressed as frictional divergence develops near the surface and reduces moisture levels there (Maloney and Hartmann 1998). Slowly, the cycle begins again as dynamic and radiative processes begin recharging the atmosphere in preparation for the next episode of intraseasonal deep convection.

7. Concluding remarks

This study focuses on a number of key elements that characterize the MJO. The results of this paper suggest that reanalysis data are suitable for use in capturing the large-scale and mesoscale features of the approach and departure of the MJO convective phase. Our approach involves utilizing time–height composites of unfiltered pentad-mean fields to examine MJO features such as the rapid postconvective, lower-tropospheric drying signal associated with horizontal winds. Abundant evidence of pre-deep-convective shallow cumulus activity and the importance of lower-tropospheric convective heating prior to maximum rainfall is noted. We also highlight unique characteristics of MJO events based on their geographic location and relative strength, and provide comments on the synthesis of wave instability theories in explaining the MJO.

Our analysis highlights the importance of shallow convective heating and moistening by cumuli prior to the arrival of the intense rainfall. One to three weeks preceding day 0, the combination of increased low-level moisture and convective vertical transport of $q' > 0$ in the lower to middle troposphere acts as a critical component in preconditioning the environment for deep convection. Near day 0, precipitation processes evolve from convective to stratiform, according to the vertical structures of Q'_1 and Q'_2 (Fig. 6a).

Following deep convection, we note a distinct vertical and temporal drying structure. The composite results indicate that there is a tendency for anomalous

horizontal winds ($\mathbf{v}_h'$) to be associated with low-level drying soon after the most intense precipitation has ended. This drying related to the initial $\mathbf{v}_h'$ maximum occurs a few days earlier than the onset of deep-layer subsidence and 1–2 weeks earlier than the most intense subsidence. Previous studies, including Hendon and Salby (1994) and Maloney and Hartmann (1998), implemented filtered data fields to analyze this delayed deep-layer subsidence and drying. While our results strongly support their findings, we note that a more immediate drying associated with horizontal advection may play an important role only a few days following intense rainfall, especially for MJO events in the Indian Ocean. This drying is possibly linked to midlevel mesoscale inflow (Houze et al. 2000).

Concerning proposed wave growth and instability theories associated with the MJO, we find that certain theories are effective in explaining specific phases of the disturbance, but no single theory can yet explain all aspects of the MJO. Our results suggest that theories outlining a gradual increase of lower-tropospheric heat and moisture that acts to destabilize the atmosphere [namely, the discharge–recharge mechanism (Bladé and Hartmann 1993; Hu and Randall 1994; Kemball-Cook and Weare 2001) and frictional-convergence feedback (Wang 1988; Salby et al. 1994; Maloney and Hartmann 1998)] are most appropriate in explaining many aspects of the observed MJO. Such preconditioning of the atmosphere via anomalous low-level warming and moistening preceding deep convection is clearly seen in the results of this study. Although certain elements of traditional wave-CISK and stratiform instability mechanisms agree with our findings, several inconsistencies prohibit a direct application of either of these theories to the observed total MJO life cycle.

Although research on the MJO is currently into its fourth decade, many aspects of this tropical disturbance remain unsolved. Continued exploration of the issues surrounding the MJO—including wave triggering mechanisms, extratropical connections, scale interactions, and cloud processes—is a vital step toward answering these questions.

Acknowledgments. We are grateful for helpful and encouraging comments from three anonymous reviewers. Both TRMM rainfall and MODIS cloud data were acquired as part of NASA's Earth Science Enterprise and were obtained from the Goddard Distributed Active Archive Center. ERA-40 data were obtained from the ECMWF data server. Gridded GPCP data were provided by NASA/GSFC's Laboratory for Atmospheres. QuikSCAT wind data were obtained from PO.DAAC at the NASA JPL. The CERES OLR data were obtained from the NASA Langley Research Center Atmospheric Sciences Data Center. This research project was funded by the Department of Energy Atmospheric Radiation Measurement program Grant DE-FG02-02ER63370, NASA Contract NNG04G125G, and National Science Foundation Grant ATM-981212384.

APPENDIX

Composite Anomaly Calculation

For all nonprecipitation variables A, each defined MJO event (i) contains a time series of that variable at all ERA-40 model pressure levels (p, 1000–200 hPa). For a fixed p, the background state $\overline{A(p)}$ from which departures are calculated is

$$\overline{A(p)} = \frac{1}{T}\sum_{i=1}^{N}\sum_{j=-30}^{+20} A(p)_i^j, \qquad \text{(A1)}$$

where i is the event counter, N the total number of events, j the lag day (or pentad) counter, and T is N multiplied by the total number of lag days (or pentads) for each event. Departures from $\overline{A(p)}$ are defined as follows:

$$[A(p)^j]' = \left(\frac{1}{N}\sum_{i=1}^{N} A(p)_i^j\right) - \overline{A(p)}, \qquad \text{(A2)}$$

where $[A(p)^j]'$ is the anomaly value for each pressure level and each lag day (or pentad).

REFERENCES

Bladé, I., and D. L. Hartmann, 1993: Tropical intraseasonal oscillations in a simple nonlinear model. *J. Atmos. Sci.,* **50,** 2922–2939.

Bony, S., and K. A. Emanuel, 2005: On the role of moist processes in tropical intraseasonal variability: Cloud-radiation and moisture–convection feedbacks. *J. Atmos. Sci.,* **62,** 2770–2789.

Cho, H.-K., K. P. Bowman, and G. R. North, 2004: Equatorial waves including the Madden–Julian oscillation in TRMM rainfall and OLR data. *J. Climate,* **17,** 4387–4406.

Cox, S. K., and K. T. Griffith, 1979: Estimates of radiative divergence during phase III of the GARP Atlantic tropical experiment: Part I. Methodology. *J. Atmos. Sci.,* **36,** 576–585.

DeMott, C. A., and S. A. Rutledge, 1998: The vertical structure of TOGA COARE convection. Part II: Modulating influences and implications for diabatic heating. *J. Atmos. Sci.,* **55,** 2748–2762.

ECMWF, cited 2003a: IFS documentation CY28r1, Part III: Dynamics and numerical procedures. ECMWF IFS documentation cycle CY28r1, Reading, United Kingdom, 38 pp. [Available online at http://www.ecmwf.int/research/ifsdocs/CY28r1/Dynamics/index.html.]

——, cited 2003b: IFS documentation CY28r1, Part IV: Physical processes. ECMWF IFS documentation cycle CY28rl, Read-

ing, United Kingdom, 175 pp. [Available online at http://www.ecmwf.int/research/ifsdocs/CY28r1/Physics/index.html.]

Emanuel, K. A., 1987: An air–sea interaction model of intraseasonal oscillations in the Tropics. *J. Atmos. Sci.,* **44,** 2324–2340.

Hayashi, Y., 1970: A theory of large-scale equatorial waves generated by condensation heat and accelerating the zonal wind. *J. Meteor. Soc. Japan,* **48,** 140–160.

Hendon, H. H., and M. L. Salby, 1994: The life cycle of the Madden–Julian oscillation. *J. Atmos. Sci.,* **51,** 2225–2237.

Houze, R. A., Jr., 1982: Cloud clusters and large-scale vertical motion in the Tropics. *J. Meteor. Soc. Japan,* **60,** 396–410.

——, 1997: Stratiform precipitation in regions of convection: A meteorological paradox? *Bull. Amer. Meteor. Soc.,* **78,** 2179–2196.

——, S. S. Chen, D. E. Kingsmill, Y. Serra, and S. E. Yuter, 2000: Convection over the Pacific warm pool in relation to the atmospheric Kelvin–Rossby wave. *J. Atmos. Sci.,* **57,** 3058–3089.

Hu, Q., and D. A. Randall, 1994: Low-frequency oscillations in radiative–convective systems. *J. Atmos. Sci.,* **51,** 1089–1099.

Huffman, G. J., R. F. Adler, M. Morrissey, D. T. Bolvin, S. Curtis, R. Joyce, B. McGavock, and J. Susskind, 2001: Global precipitation at one-degree daily resolution from multisatellite observations. *J. Hydrometeor.,* **2,** 36–50.

Johnson, R. H., and G. S. Young, 1983: Heat and moisture budgets of tropical mesoscale anvil clouds. *J. Atmos. Sci.,* **40,** 2138–2147.

——, P. E. Ciesielski, and K. A. Hart, 1996: Tropical inversions near the 0°C level. *J. Atmos. Sci.,* **53,** 1838–1855.

Jones, C., and B. C. Weare, 1996: The role of low-level moisture convergence and ocean latent heat fluxes in the Madden and Julian oscillation: An observational analysis using ISCCP data and ECMWF analyses. *J. Climate,* **9,** 3086–3104.

Källberg, P., cited 1998: Aspects of the re-analysed climate. ERA-15 Project Report Series 2, ECMWF, Reading, United Kingdom, 96 pp. [Available online at http://www.ecmwf.int/publications/library/do/references/list/191.]

Kemball-Cook, S. R., and B. C. Weare, 2001: The onset of convection in the Madden–Julian oscillation. *J. Climate,* **14,** 780–793.

Kikuchi, K., and Y. N. Takayabu, 2004: The development of organized convection associated with the MJO during TOGA COARE IOP: Trimodal characteristics. *Geophys. Res. Lett.,* **31,** L10101, doi:10.1029/2004GL019601.

Kiladis, G. N., K. H. Straub, and P. T. Haertel, 2005: Zonal and vertical structure of the Madden–Julian oscillation. *J. Atmos. Sci.,* **62,** 2790–2809.

King, M., and Coauthors, 2003: Cloud and aerosol properties, precipitable water, and profiles of temperature and water vapor from MODIS. *IEEE Trans. Geosci. Remote Sens.,* **41,** 442–458.

Kummerow, C., and Coauthors, 2000: The status of the Tropical Rainfall Measuring Mission (TRMM) after two years in orbit. *J. Appl. Meteor.,* **39,** 1965–1982.

Lau, K.-M., and L. Peng, 1987: Origin of low-frequency (intraseasonal) oscillations in the tropical atmosphere. Part I: Basic theory. *J. Atmos. Sci.,* **44,** 950–972.

——, and D. E. Waliser, 2005: *Intraseasonal Variability in the Atmosphere–Ocean Climate System.* Praxis Publishing Ltd., 436 pp.

Lin, J.-L., M. Zhang, and B. Mapes, 2005: Zonal momentum budget of the Madden–Julian oscillation: The source and strength of equivalent linear damping. *J. Atmos. Sci.,* **62,** 2172–2188.

——, and Coauthors, 2006: Tropical intraseasonal variability in 14 IPCC AR4 climate models. Part I: Convective signals. *J. Climate,* **19,** 2665–2690.

Lin, X., and R. H. Johnson, 1996a: Kinematic and thermodynamic characteristics of the flow over the western Pacific warm pool during TOGA COARE. *J. Atmos. Sci.,* **53,** 695–715.

——, and ——, 1996b: Heating, moistening, and rainfall over the western Pacific warm pool during TOGA COARE. *J. Atmos. Sci.,* **53,** 3367–3383.

Lindzen, R. S., 1974: Wave-CISK in the Tropics. *J. Atmos. Sci.,* **31,** 156–179.

Luo, H., and M. Yanai, 1984: The large-scale circulation and heat sources over the Tibetan Plateau and surrounding areas during the early summer of 1979. Part II: Heat and moisture budgets. *Mon. Wea. Rev.,* **112,** 966–989.

Madden, R. A., and P. R. Julian, 1971: Detection of a 40–50 day oscillation in the zonal wind in the tropical Pacific. *J. Atmos. Sci.,* **28,** 702–708.

——, and ——, 1972: Description of global-scale circulation cells in the Tropics with a 40–50 day period. *J. Atmos. Sci.,* **29,** 1109–1123.

——, and ——, 1994: Observations of the 40–50-day tropical oscillation—A review. *Mon. Wea. Rev.,* **122,** 814–837.

Maloney, E. D., and D. L. Hartmann, 1998: Frictional moisture convergence in a composite life cycle of the Madden–Julian oscillation. *J. Climate,* **11,** 2387–2403.

Mapes, B. E., 2000: Convective inhibition, subgrid-scale triggering energy, and stratiform instability in a toy tropical wave model. *J. Atmos. Sci.,* **57,** 1515–1535.

Masunaga, H., T. S. L'Ecuyer, and C. D. Kummerow, 2006: The Madden–Julian oscillation recorded in early observations from the Tropical Rainfall Measuring Mission (TRMM). *J. Atmos. Sci.,* **63,** 2777–2794.

Matthews, A. J., and J. Lander, 1999: Physical and numerical contributions to the structure of Kelvin wave-CISK modes in a spectral transform model. *J. Atmos. Sci.,* **56,** 4050–4058.

Morita, J., Y. Takayabu, and S. Shige, 2006: Analysis of rainfall characteristics of the Madden–Julian oscillation using TRMM satellite data. *Dyn. Atmos. Oceans,* **42,** 107–126.

Myers, D. S., and D. E. Waliser, 2003: Three-dimensional water vapor and cloud variations associated with the Madden–Julian oscillation during Northern Hemisphere winter. *J. Climate,* **16,** 929–950.

Platnick, S., M. King, S. Ackerman, P. Menzel, B. Baum, J. Riédi, and R. Frey, 2003: The MODIS cloud products: Algorithms and examples from terra. *IEEE Trans. Geosci. Remote Sens.,* **41,** 459–473.

Reed, R. J., and E. E. Recker, 1971: Structure and properties of synoptic-scale wave disturbances in the equatorial western Pacific. *J. Atmos. Sci.,* **28,** 1117–1133.

Rui, H., and B. Wang, 1990: Development characteristics and dynamic structure of tropical intraseasonal convection anomalies. *J. Atmos. Sci.,* **47,** 357–379.

Salby, M. L., R. R. Garcia, and H. H. Hendon, 1994: Planetary-scale circulations in the presence of climatological and wave-induced heating. *J. Atmos. Sci.,* **51,** 2344–2367.

Sperber, K. R., 2003: Propagation and the vertical structure of the Madden–Julian oscillation. *Mon. Wea. Rev.,* **131,** 3018–3037.

Stephens, G. L., P. J. Webster, R. H. Johnson, R. Engelen, and T. L'Ecuyer, 2004: Observational evidence for the mutual regu-

lation of the tropical hydrological cycle and tropical sea surface temperatures. *J. Climate,* **17,** 2213–2224.

Straub, K. H., and G. N. Kiladis, 2003: The observed structure of convectively coupled Kelvin waves: Comparison with simple models of coupled wave instability. *J. Atmos. Sci.,* **60,** 1655–1668.

Wang, B., 1988: Dynamics of tropical low-frequency waves: An analysis of the moist Kelvin wave. *J. Atmos. Sci.,* **45,** 2051–2065.

Weickmann, K. M., G. R. Lussky, and J. E. Kutzbach, 1985: Intraseasonal (30–60 day) fluctuations of outgoing longwave radiation and 250 mb streamfunction during northern winter. *Mon. Wea. Rev.,* **113,** 941–961.

Wheeler, M., and G. N. Kiladis, 1999: Convectively coupled equatorial waves: Analysis of clouds and temperature in the wavenumber–frequency domain. *J. Atmos. Sci.,* **56,** 374–399.

Woolnough, S. J., J. M. Slingo, and B. J. Hoskins, 2000: The relationship between convection and sea surface temperature on intraseasonal timescales. *J. Climate,* **13,** 2086–2104.

Wu, Z., 2003: A shallow CISK, deep equilibrium mechanism for the interaction between large-scale convection and large-scale circulations in the Tropics. *J. Atmos. Sci.,* **60,** 377–392.

Yanai, M., S. Esbensen, and J.-H. Chu, 1973: Determination of bulk properties of tropical cloud clusters from large-scale heat and moisture budgets. *J. Atmos. Sci.,* **30,** 611–627.

Zhang, C., 2005: Madden-Julian Oscillation. *Rev. Geophys.,* **43,** RG2003, doi:10.1029/2004RG000158.

——, and M. J. McPhaden, 2000: Intraseasonal surface cooling in the equatorial west Pacific. *J. Climate,* **13,** 2261–2276.